5

REMOTE SENSING OF DRY SNOW

This Chapter is dedicated to analysis of the use of GNSS-R for remote sensing of thick dry snow masses. Motivated by the preliminary results shown in previous Section 3.3, where the reflected waveforms off Antarctic dry snow appear to be composed by surface and sub-surface contributions, Section 5.1 describes the forward model developed to simulate such behavior and then to infer information from the data such as the depth from the contributing layers. The results obtained towards this purpose and further work are shown in Section 5.2. Table 19 provides a list of publications issued from the study presented along this Chapter.

Most relevant **novelty** with respect to previous GNSS-R studies: **Empirical remote sensing of deep dry snow layers based on multiple reflections.**

Title	**Reference**
Monitoring sea ice and dry snow with GNSS reflections	Fabra et al. (2010)
An empirical approach towards characterization of dry snow layers using GNSS-R	Fabra et al. (2011a)
GNSS Reflectometry for the remote sensing of sea ice and dry snow	Fabra et al. (2011d)
GNSS-R for the Retrieval of Internal Layers' Information from Dry Snow Masses	Fabra et al. (2011c)
Characterization of Dry-snow Sub-structure using GNSS Reflected Signals	Cardellach et al. (2012)
Sun reflections off Antarctica's snow sub-structural layers	In preparation for *Geophysical Research Letters*

Table 19.: List of publications arisen from the work presented in this Chapter.

5.1 MODELING AND PROCESSING GNSS-R OVER DRY SNOW: A NOVEL APPROACH

5.1.1 PROPERTIES OF THE REFLECTED SIGNALS

The received reflected signals from this experiment present coherence times longer than 1 second. This is a very long coherence time compared to GNSS signals reflected off other types of surfaces. For instance, reflections off the rough ocean present several millisecond coherence only. Part of this long coherence time can be understood by the fact that the receiver cross-correlates the reflected signals with a signal model that includes real-time information obtained by the direct radio-link. In other words, the receiver tends to stop the reflected signal using the dynamics of the direct one. The other factor to understand the long coherence is the fact that the snow surface is very smooth and the scattering is essentially specular. The snow surface topography in the area is essentially flat, with global slope $< 0.2^\circ$, and roughness characterized by very long auto-correlation length (compared to GPS electromagnetic wavelengths) and $\sim$1 cm RMS vertical dispersion (Petit et al., 1982; Six et al., 2004). That is, the surface roughness is not large enough to induce diffuse scattering, which would have introduced fluctuation in the phase.

Specular reflections tend to generate waveforms with the shape of the signal modulation's auto-correlation function, with no further deformations (in opposition to diffuse scattering). The received waveforms, nevertheless, do not show the expected triangle shape from the GPS C/A code ($2\rho_{\mathrm{C/A}} \simeq 600$ m width in the space domain), but a series of distorted triangles, with added tails and secondary peaks. Moreover, these shapes change gradually in time, as displayed in Figure 74. We can see that the reflected waveforms are not constant, but oscillate, and that these oscillations differ between distant lags.

An example of the amplitude oscillation pattern found is given in Figure 75: a short time series is chosen to perceive the high rate components of the interference and their repeatability. It shows a sequence of 1-second integrated amplitudes for two different lags and four different days: lag 22, which approximately corresponds to the peak of the direct waveform (nominal zero delay); and lag 37, delayed by $\sim$225 meter (see Figure 74 to locate both lags within the waveform). The oscillation patterns at lag 22 and lag 37 present similarities, but do not perfectly match with each other. Further delayed lags tend to slightly increase the rate: double peaks appear sometimes where only one peak was detected in lag 22. For example, it happens around elevation $\sim 44.65^\circ$, $\sim 44.9^\circ$, or $\sim 45.28^\circ$. We could think those are effects of the noise (lower SNR levels at the end of the trailing edge, lag 37), however, some of these new peaks have significant SNR levels, and a hint of them seemed to emerge in lag 22. Moreover, all days present the same patterns, thus suggesting that they cannot be just noise, but some signal.

In the GNSS geodesy community the term multipath designates a particular type of reflections, near the receiving system (Elósegui et al., 1995; Byun et al., 2002). Multipath is usually an undesired effect which might mask or deteriorate the GNSS observables, because it interferes with the main ray generating oscillating patterns in the amplitude and the phase, as it happened in Greenland's campaign for sea ice remote sensing, whose data analysis was described in Chapter 4. The frequency of these patterns is given by

$$f_M = \frac{-1}{\lambda} \frac{d\rho_M}{dt} \tag{65}$$

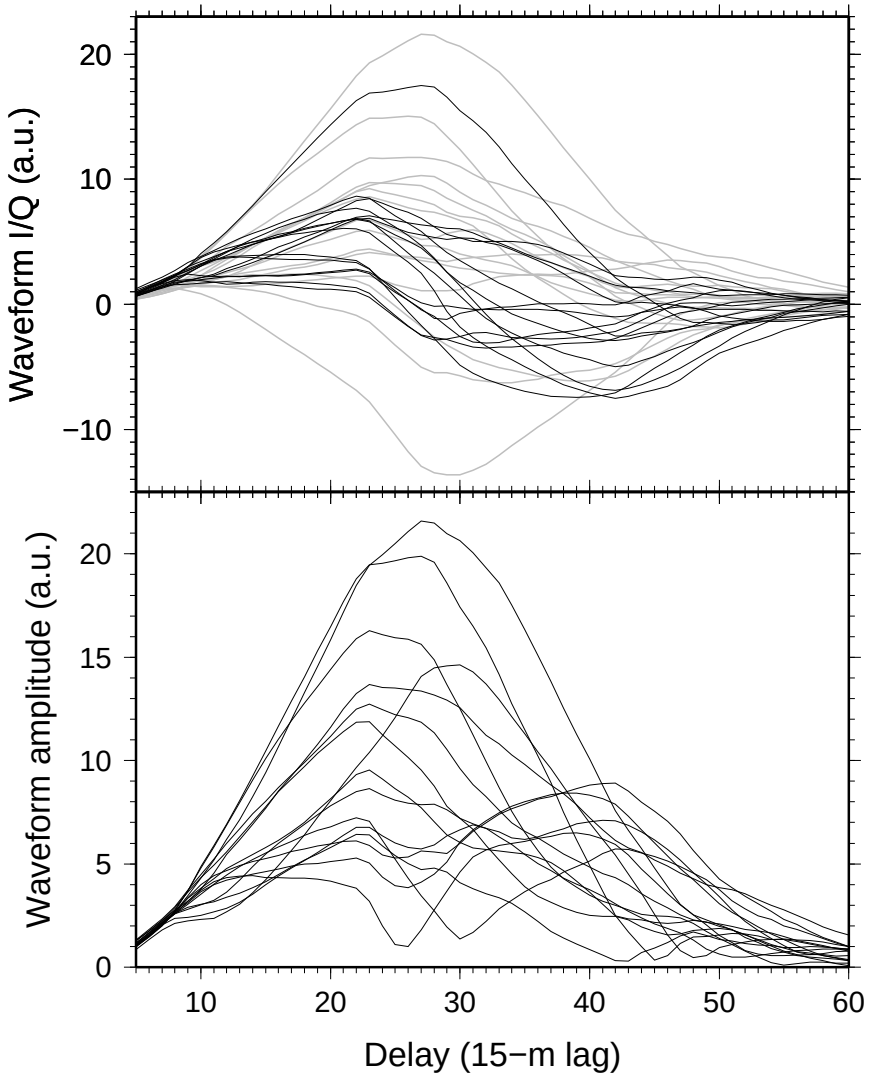

Figure 74.: Amplitudes of a sequence of 1-second integrated complex waveforms collected with the GOLD-RTR receiver (PRN 13, December 16, 2009), between 44.5° and 45.5° elevation (only 1 out of every 10 waveforms are here shown, to avoid overloading the plot). [Top] In-phase and Quadrature components (in gray and black respectively). [Bottom] Total amplitude. Figure from Cardellach et al. (2012).

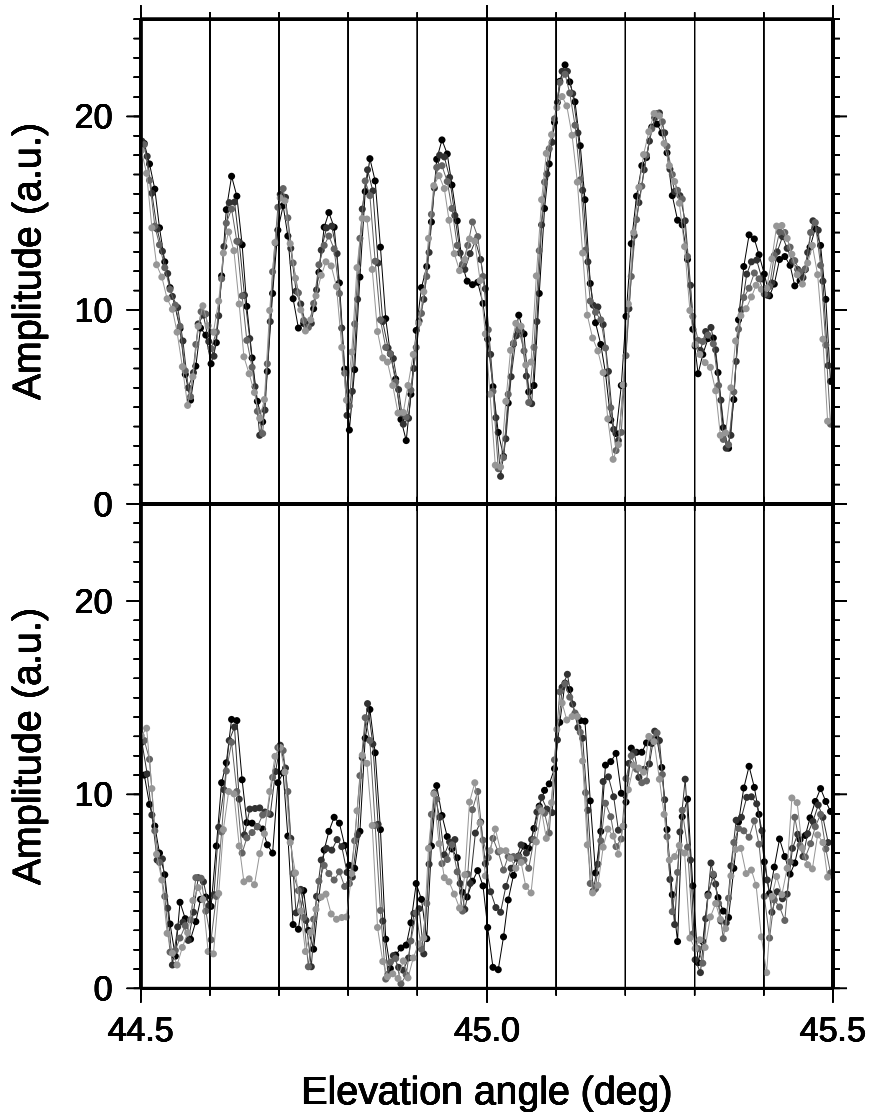

Figure 75.: Amplitude of lag-22 (top) and lag-37 (bottom) of the 1-second integrated waveforms, between 44.5° and 45.5° elevation, for PRN 13. Days 16 to 19 December 2009 have been plotted in different hues of grey. Note that some of these points are explicitly contained in the bottom panel in Figure 74 (December 16). Figure from Cardellach et al. (2012).

where ρ_M is the range delay between the reflected and the direct signals; and λ is the electromagnetic wavelength of the signal. Assuming planar horizontal reflectors, the phase with which the multipath signal reaches the receiver, measured in cycles with respect to the phase of the main signal, can be modeled as

$$\Phi_M = \frac{\rho_M}{\lambda} = \frac{2H_M}{\lambda}\sin(\varepsilon) \tag{66}$$

being ε the elevation angle of observation, and H_M the vertical distance at which the reflecting surface is located with respect to the receiving antenna. Note that this expression is consistent with previous Equation (33) after taken into account the radian-to-cycles conversion. The multipath field sums coherently with the main field, with a rotated phase with respect to the main signal as given in Equation (66). As the conditions change (either H_M or the elevation angle of observation ε), the multipath phase in Equation (66) changes too, introducing a rotation of the added field with respect to the main one. This phenomena introduces oscillations in both amplitude and phase. In our experimental set-up, the only dynamic parameter is the elevation angle. As will be shown later, the rate of change of the elevation angle of observation is too low for a near-by reflector (or even from the shelter at the base of the tower) to introduce the scintillating patterns observed in the data. A near-by multipath phenomena, thus, cannot be the source of interference.

In the GNSS radio-occultation community, the term multipath, or tropospheric multipath, is applied to the phenomena that occurs under certain atmospheric conditions, for which the GNSS signals split in several rays. A technique called radio-holography is then used in GNSS radio-occultations to identify and separate atmospheric multipath (Igarashi et al., 2000). Similarly, a new radio-holographic observable will be later introduced in Section 5.1.3 to shed some light on the source of the patterns.

5.1.2 FORWARD MODEL: MULTIPLE-RAY SINGLE-REFLECTION

Rays may be reflected off both the external snow surface and internal snow interfaces. Given the clear multiple interference patterns observed in the data, we have neglected volumetric scattering (contrary to work done by Wiehl et al. (2003)), which would not produce interference patterns, and we have focused on scattering off internal layers. We have taken a geometrical optics approach, where the different contributions are modeled as rays bouncing in different layers. A general view of the components of the model we implemented are sketched in Figure 76. We assume locally horizontal layers, parallel incidence, and propagation/reflection through the snow layers following the Snell's law:

$$n_{(i+1)} \sin\theta_{(i+1)} = n_i \sin\theta_i \tag{67}$$

where θ_i is the incidence angle and n_i is the refractive index of the i-layer. The permittivity profiles, previously shown in Figure 29 from Chapter 3, are computed from the in-situ dry snow measurements described in Appendix E.3. The model considers a set of rays contributing to the total received signal, where each ray might suffer single-reflections solely, so we call it Multiple-Rays Single-Reflection (MRSR) model.

The following sub-sections will describe the equations of the delay ρ_i (Section 5.1.2.1) and the amplitude U_i (Section 5.1.2.2) with which a field that incises into the snow, propagates down to the i-layer, rebounds, and propagates back to the snow-air interface, finally reaches the receiver. With this information, the complex waveform receiver can be constructed (Section 5.1.2.3).

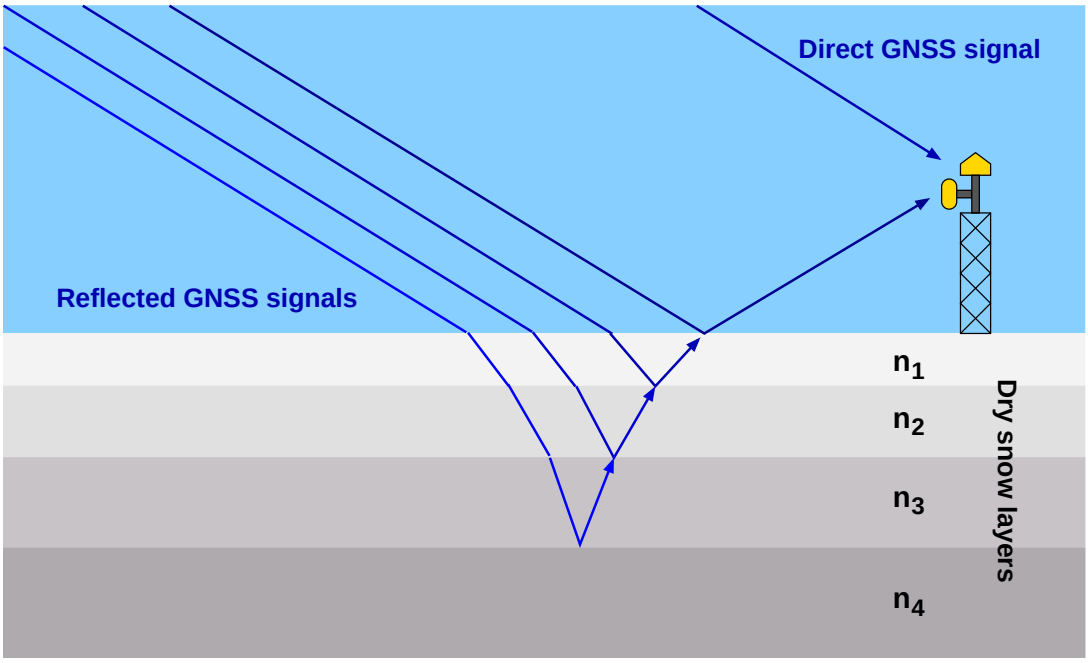

Figure 76.: Basic scheme of the multiple-ray single-reflection model (MRSR).

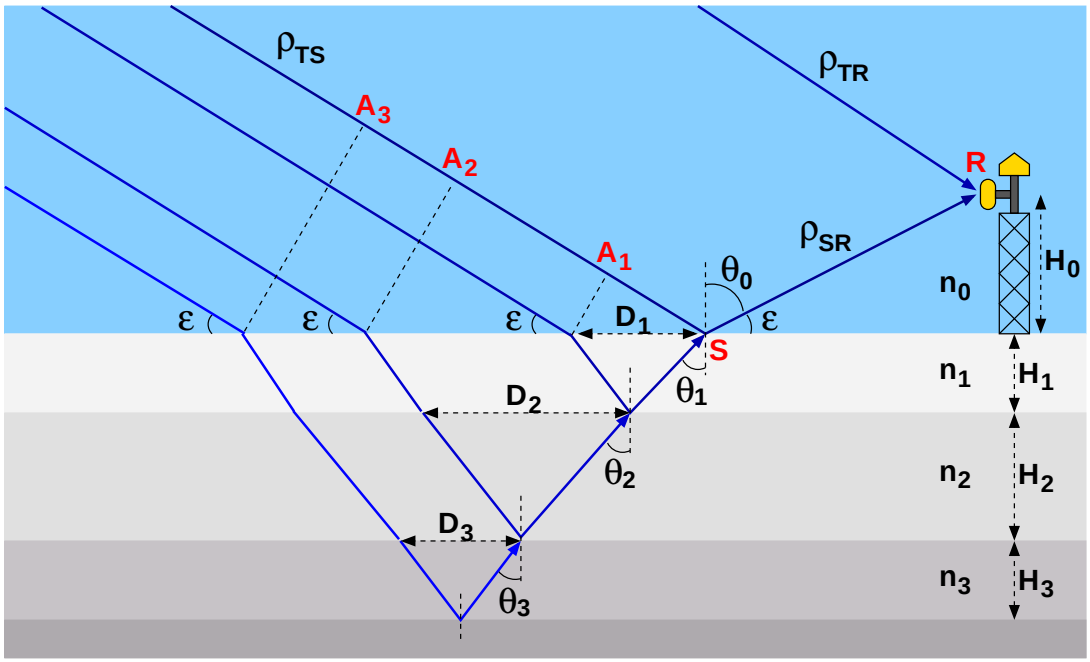

Figure 77.: Sketch of the single-reflection approach implemented to model the snow internal reflections. Each layer has a constant refractive index n_i.

5.1.2.1 *Delay of the i-layer contribution*

The first step of the model is to compute, for each i-layer, the delay of the ray such that manages to propagate down into the i-layer, is reflected off the bottom of that layer, and propagates upward towards the receiver. These delays, ρ_i, are given with respect to the direct reception of the signal (radio-link from the transmitter to the receiver with no reflection). As described below, most of the contributions to the i-delay are also common to the rays that have been reflected from the layers above it. Therefore, an iterative approach can easily solve the problem. In our notation 0-layer is the external air, so the 0-delay corresponds to the reflection off the snow's external surface (point **S** in Figure 77):

$$\rho_0 = \rho_{TS} + \rho_{SR} - \rho_{TR} \tag{68}$$

where subscripts TS, SR, and TR mean Transmitter-Specular reflection point, Specular reflection point-Receiver, and Transmitter-Receiver (direct radio-link) respectively. Note that in this case, ρ_0 is equivalent to ρ_{geo} in the notation employed during the analysis of sea ice described in Chapter 4, where only surface reflections were under study. The ray which propagates into the first layer of snow, of refractive index n_1, and gets reflected off of its bottom, is delayed with respect to the direct-link by ρ_1. This delay has several contributions: (1) the one given by the internal propagation through layer 1, ρ_{int-1}; (2) the distance from the specular point to the receiver, ρ_{SR}; (3) the distance from the transmitter to the point in which this ray enters the snow. This distance is equal to the distance between the transmitter and the specular reflection point, except for the segment between A_1 and the specular point **S**; (4) finally, in order to reference the delay to the direct radio-

link reception, we need to subtract the direct distance between the transmitter and the receiver, ρ_{TR}. These four contributions are summarized in the following equation:

$$\rho_1 = \rho_{int-1} + \rho_{SR} + [\rho_{TS} - \overline{A_1 S}] - \rho_{TR} \tag{69}$$

where

$$\rho_{int-1} = 2n_1 \frac{H_1}{\cos(\theta_1)} \tag{70}$$

and

$$\overline{A_1 S} = D_1 \sin(\theta_0) \tag{71}$$

D_1 being the horizontal extent of the propagation inside the 1-layer of snow (see Figure 77):

$$D_1 = 2H_1 \tan(\theta_1) \tag{72}$$

A compact way to express it is:

$$\rho_1 = \rho_0 + \rho_{int-1} - D_1 \sin(\theta_0) \tag{73}$$

Similarly, the ray that manages to propagate down to layer-2, get reflected off its bottom, and propagate upward to reach the receiver is:

$$\rho_2 = \rho_{int-2} + \rho_{int-1} + \rho_{SR} + [\rho_{TS} - \overline{A_2 S}] - \rho_{TR} \tag{74}$$

where ρ_{int-2} is the delay-contribution from the internal propagation through layer-2

$$\rho_{int-2} = 2n_2 \frac{H_2}{\cos(\theta_2)} \tag{75}$$

and the distance between the specular point $\mathbf{S}$ and the point $\mathbf{A_2}$, $\overline{A_2 S}$, is:

$$\overline{A_2 S} = (D_1 + D_2) \sin(\theta_0) \tag{76}$$

being $D_2 = 2H_2 \tan(\theta_2)$.

To complete these examples, the 3rd layer would read:

$$\rho_3 = \rho_{int-3} + \rho_{int-2} + \rho_{int-1} + \rho_{SR} + [\rho_{TS} - (D_1 + D_2 + D_3) \sin(\theta_0)] - \rho_{TR} \tag{77}$$

with

$$\rho_{int-3} = 2n_3 \frac{H_3}{\cos(\theta_3)} \tag{78}$$

and $D_3 = 2H_3 \tan(\theta_3)$.

Therefore, the general expression for the i-layer is:

$$\rho_i = \rho_0 + \sum_{k=1}^{k=i} 2n_k \frac{H_k}{\cos(\theta_k)} - \left(\sum_{k=1}^{k=i} D_k \right) \sin(\theta_0) \tag{79}$$

being

$$D_k = 2H_k \tan(\theta_k) \tag{80}$$

Figure 78 shows the delay at which the signals reflected off each snow layer reach the receiver when considering the permittivity profile displayed in Figure 29.

Note that because the incidence angle of the observation constantly evolves in time, the delay between the direct and reflected signals also changes in time. A receiver *tracking* the direct direct signal but receiving a contribution from another ray-path from a reflection off the i-layer, does not *lock* this other component because the latter arrives with a different frequency. This interferometric frequency (with respect to the direct one) has a multipath-like behavior and therefore can be computed using Equation (65).

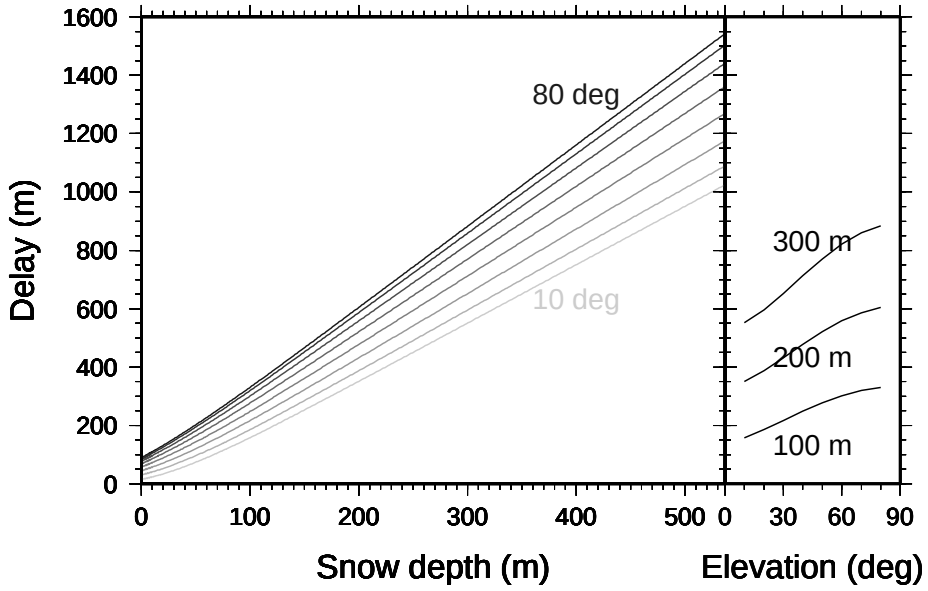

Figure 78.: A ray propagating into the snow, down to the x-meter depth layer, reflected at that layer, and propagated upward to reach the receiver, arrives with y-delay with respect to the direct signal (according to the model in Equation (79)). The delay depends on the elevation angle of observation: grey hues, from 10° to 80° elevation, in steps of 10°, lighter to darker respectively. The dependency on the elevation angle is also shown on the right frame, where the delays in the signals reflected by layers 100, 200, and 300 meter deep are plotted as function of the elevation angle. Figure from Cardellach et al. (2012).

5.1.2.2 *Amplitude of the i-layer contribution*

The next step in the MRSR model is to estimate the amplitude with which the ray reflected off of the bottom of the *i*-layer would reach the receiver. The incident field at the surface level is normalized to 1. We will take into account:

- The transmission and reflection Fresnel coefficients, $\mathcal{T}$ and $\Re$.
- The propagation attenuation within each snow layer (attenuation coefficient α), but not along the air propagation.

The equations are extracted from Ulaby et al. (1990c), and modified to depend on the angle in the incident medium. This modification uses trigonometry, the Snell's law, and assumes non-magnetic mediums:

$$k_1 \sin\theta_1 = k_2 \sin\theta_2 \tag{81}$$
$$\sqrt{\epsilon_1}\sin\theta_1 = \sqrt{\epsilon_2}\sin\theta_2 \tag{82}$$

where k_i is the wavenumber and θ_i the incidence angle from the normal direction in the *i*-medium. The modified expressions read:

$$\mathcal{T}_\perp = \frac{2\cos\theta_1}{\cos\theta_1 + \sqrt{\frac{\epsilon_2}{\epsilon_1} - \sin^2\theta_1}} \tag{83}$$
$$\mathcal{T}_\parallel = \frac{2\cos\theta_1}{\cos\theta_1 + \sqrt{\frac{\epsilon_1}{\epsilon_2} - (\frac{\epsilon_1}{\epsilon_2}\sin\theta_1)^2}} \tag{84}$$

$$\Re_\perp = \frac{\epsilon_1\cos\theta_1 - \sqrt{\epsilon_1\epsilon_2 - (\epsilon_1\sin\theta_1)^2}}{\epsilon_1\cos\theta_1 + \sqrt{\epsilon_1\epsilon_2 - (\epsilon_1\sin\theta_1)^2}} \tag{85}$$
$$\Re_\parallel = \frac{\epsilon_2\cos\theta_1 - \sqrt{\epsilon_1\epsilon_2 - (\epsilon_1\sin\theta_1)^2}}{\epsilon_2\cos\theta_1 + \sqrt{\epsilon_1\epsilon_2 - (\epsilon_1\sin\theta_1)^2}} \tag{86}$$

The transmitted GPS signals are essentially Right-Hand Circular Polarized (RHCP). In order to obtain the Reflection and Transmission coefficients for circularly polarized signals, the following combinations are required:

$$\mathcal{T}_{co} = \frac{1}{2}(\mathcal{T}_\parallel + \mathcal{T}_\perp) \tag{87}$$
$$\mathcal{T}_{cross} = \frac{1}{2}(\mathcal{T}_\parallel - \mathcal{T}_\perp) \tag{88}$$
$$\Re_{co} = \frac{1}{2}(\Re_\parallel + \Re_\perp) \tag{89}$$
$$\Re_{cross} = \frac{1}{2}(\Re_\parallel - \Re_\perp) \tag{90}$$

where subindexes *co* and *cross* relate to circular co-polar and cross-polar transitions respectively.

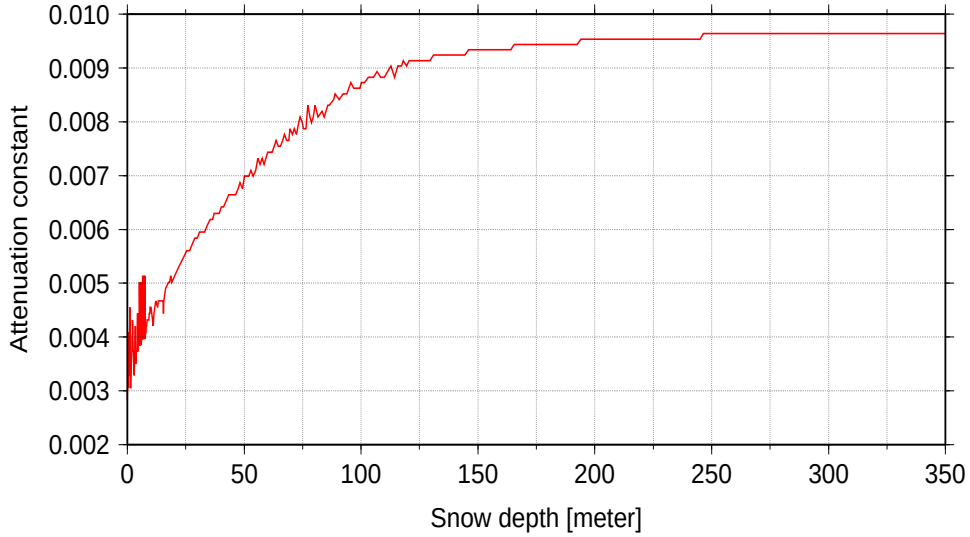

Figure 79.: Attenuation constant, α as defined in Equation (26), corresponding to the snow density profile given in Figure 134.

The internal reflection requires to model signal propagating down-ward as well as upward. We explicitly indicate the medium/layer from which the signal incises noting $\mathcal{T}_{ij}$ as the transmission coefficient where the incident layer/medium is i and the medium into which the signal propagates is j. Similarly, $\Re_{ij}$ refers to the coefficient of a reflection signal incident from medium/layer i off the interface with medium/layer j. Note that the opposite notation might be found in the literature.

The coefficients given above relate the amplitude of the transmitted/reflected field with respect to the incident field. In addition to these effects, the medium will also attenuate the signal, as discussed in Section 2.1.3.1. The attenuation constant (defined in Equation (26)) at each layer of snow when considering the permittivity profile displayed in Figure 29, is shown in Figure 79.

Given the little amount of signal transmitted to the cross-polar component (less than 0.1% of the power transmitted in the co-polar component), and the fact that only 1-reflection per ray is being considered in this model (therefore need to switch from RHCP to LHCP to be captured at the receiver LHCP antenna), we will not take into account:

- The cross-polar component of the transmitted signals.
- The co-polar component of the reflected signals.
- The geometrical loss due to the small differences between the distances traveled through open-air by different rays.

The sketch of the multi-layered snow with the amplitude factors affecting each segment of the propagation is shown in Figure 80. As mentioned above, we will consider only $\Re_{cross}$ and $\mathcal{T}_{co}$. Therefore, the $\Re$ in the figure and in the following analysis must be understood as $\Re_{cross}$ and the $\mathcal{T}$ as $\mathcal{T}_{co}$. This model is intended for the signal received with the LHCP antenna. To obtain the model for the signal received with the RCHP antenna we only would need to replace $\Re_{cross}$ by $\Re_{co}$ in the analysis below.

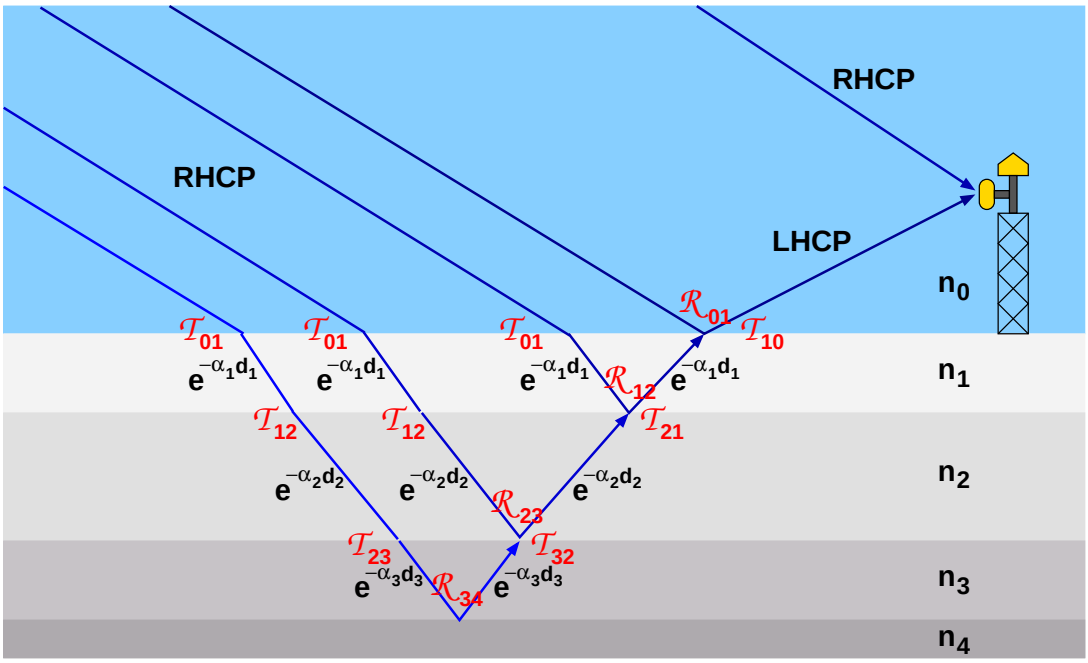

Figure 80.: Sketch of the single-reflection approach implemented to model the snow internal reflections, amplitude factors affecting each segment.

The LHCP ray reflected at the external surface will have an amplitude relative to the incident RHCP field as

$$U_0 = \Re_{01} \tag{91}$$

The one coming from a single reflection off of the bottom of the first internal layer will have an amplitude (w.r.t. incident RHCP field at the surface)

$$U_1 = \mathcal{T}_{01} e^{-\alpha_1 d_1} \Re_{12} e^{-\alpha_1 d_1} \mathcal{T}_{10} = \Re_{12} \mathcal{T}_{01} \mathcal{T}_{10} e^{-2\alpha_1 d_1} \tag{92}$$

where d_1 is the one-way physical distance traveled inside the first layer:

$$d_1 = \frac{H_1}{\cos(\theta_1)} = \frac{\rho_{int-1}}{2n_1} \tag{93}$$

Note that $\mathcal{T}_{01} \neq \mathcal{T}_{10}$, but they both must be computed interchanging the corresponding angles and permittivities.

The amplitude of the LHCP signal that has been single-reflected in the second layer would be:

$$U_2 = \mathcal{T}_{01} e^{-\alpha_1 d_1} \mathcal{T}_{12} e^{-\alpha_2 d_2} \Re_{23} e^{-\alpha_2 d_2} \mathcal{T}_{21} e^{-\alpha_1 d_1} \mathcal{T}_{10} \tag{94}$$

which can be expressed as:

$$U_2 = \Re_{23} \Pi_{i=1}^{i=2} \mathcal{T}_{(i-1)i} \mathcal{T}_{i(i-1)} e^{-2\alpha_i d_i} \tag{95}$$

It is straightforward to derive the amplitude of the contribution coming from the kth layer:

$$U_k = \Re_{k,k+1} \Pi_{i=1}^{i=k} \mathcal{T}_{(i-1)i} \mathcal{T}_{i(i-1)} e^{-2\alpha_i d_i} \tag{96}$$

Figure 81 shows the amplitude with which the signals reflected off each snow layer reach the receiver when considering the permittivity profile displayed in Figure 29.

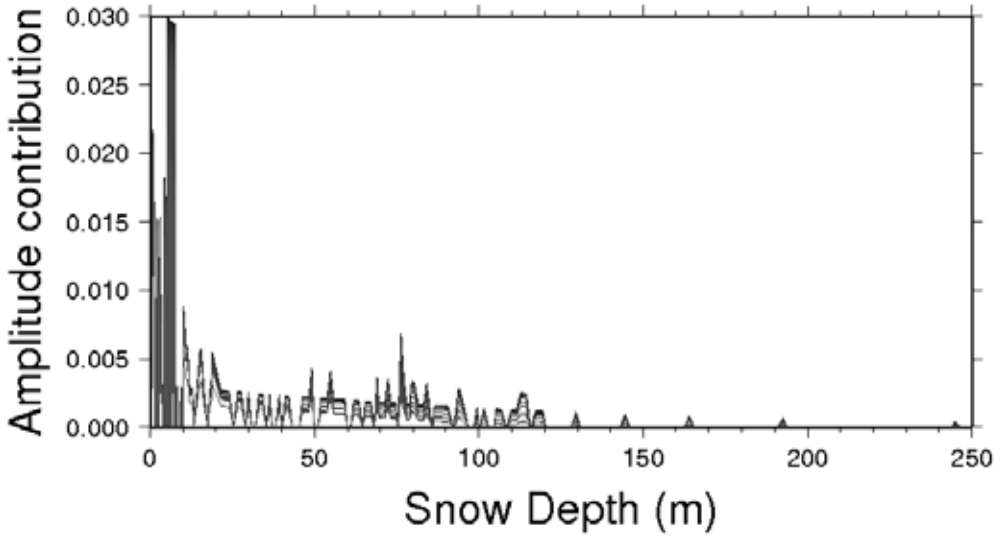

Figure 81.: Amplitude (with respect to surface incidence RHCP signal) of the contribution to the received field, coming from the single-reflection off the layer at a given altitude. Different colors for different surface incidence angles (dark to light for 10° to 80° incidence angle respectively).

5.1.2.3 *Building the complex waveforms*

The received complex waveform can be modeled by summing up the contributions from each layer. The *i*-layer contribution can be obtained as the GPS C/A auto-correlation function (triangle function) shift by the delay at which the *i*-layer reflected signal arrives (with respect to the direct signal), ρ_i defined in Equation (79), and multiplied by the amplitude corresponding to the *i*-layer, U_i defined in Equation (96). Figure 82 sketches this approach of building the total complex waveform. Moreover, this contribution will reach the receiver with a different phase than the direct signal. The phase is given by

$$\phi_i = 2\pi \frac{\rho_i}{\lambda} \tag{97}$$

We aim to produce waveforms using the same sampling than our experimental data collected with the GOLD-RTR receiver. This receiver produce complex waveform of 64 lags, 15 meter inter-lag distance. Using this sampling, the GPS C/A code has a chip width of ± 20 lags. In the case of the GPS-SIDS-DS experiment, the direct signal was set to lag 22. To express the delay of a given *i*-layer contribution, ρ_i, in lags:

$$\rho_i^{lag} = round\left\{\frac{\rho_i}{15}\right\} + 22 \tag{98}$$

Therefore, the lag τ_w of the modeled complex waveform will consist of

$$\widehat{w_r}(\tau_w) = \widehat{w_d}(\tau_w) + \sum_{k=0}^{N_{layers}} \left(\left(1.0 - \frac{|\rho_k^{lag} - \tau_w|}{20} \right) U_k e^{i\phi_k} \right) \tag{99}$$

where $\widehat{w_d}$ is the GPS C/A triangle function centered at lag 22 (corresponding to leakages of LHCP direct signal), and i is the complex unity ($i = \sqrt{-1}$).

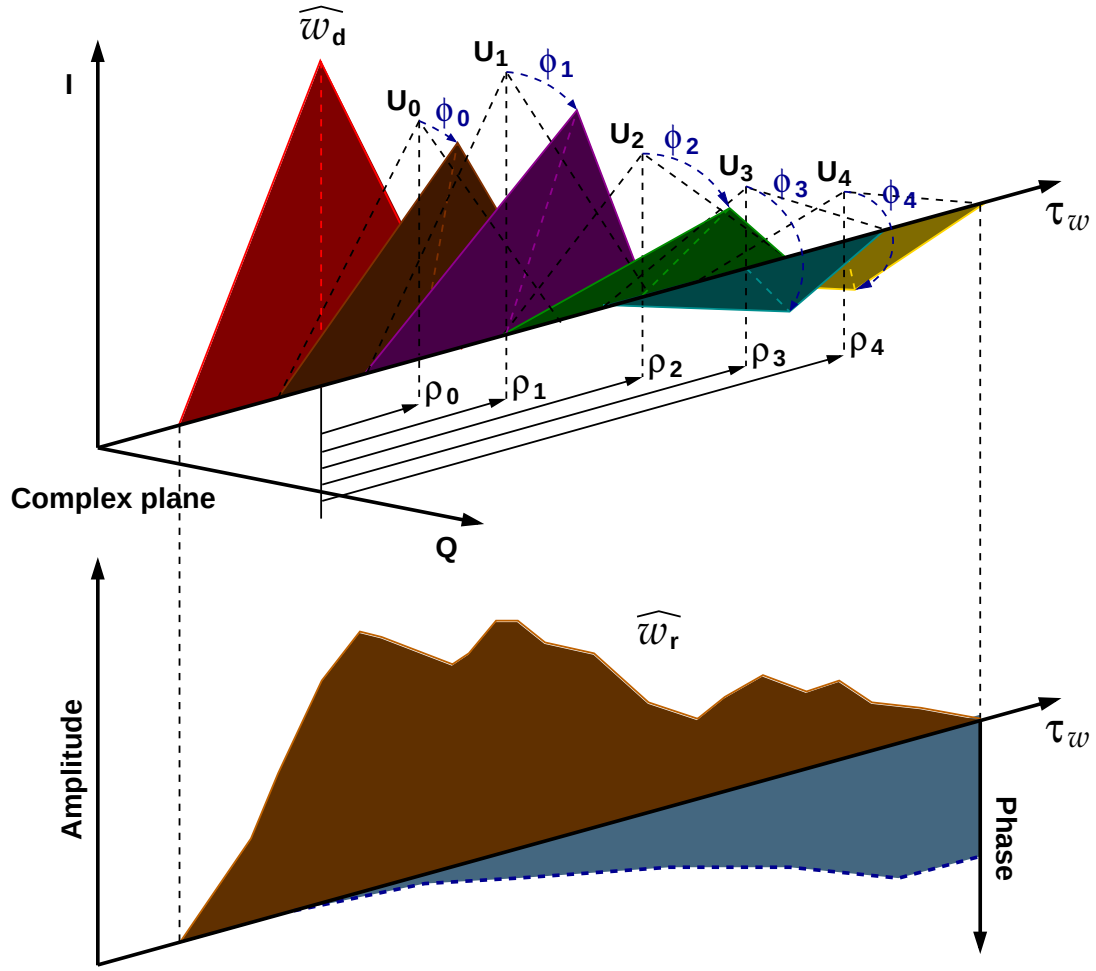

Figure 82.: Sketch of the procedure to build the total received complex waveform, once the amplitude U_i and the delay ρ_i of the contribution from each i-layer have been calculated. The phases ϕ_i depend on the delays ρ_i as indicated in Equation (97). The signal modulation is accounted, by means of triangle functions.

An example of several waveforms synthesized with this model are compiled in Figure 83. The series represents sequential complex waveforms (their real and imaginary parts) generated under identical geometric conditions as those real waveforms in Figure 74. The two figures present similar features, *folding* and *unfolding* of the waveform defining oscillating peaks and troughs, consistent with interferometric patterns given by the layered-model. If anything, the model results are more conservative than the extreme features found in the real data. Varying the contamination level of the direct signal ($\widehat{w_d}$ in Equation (99)) might improve this performance.

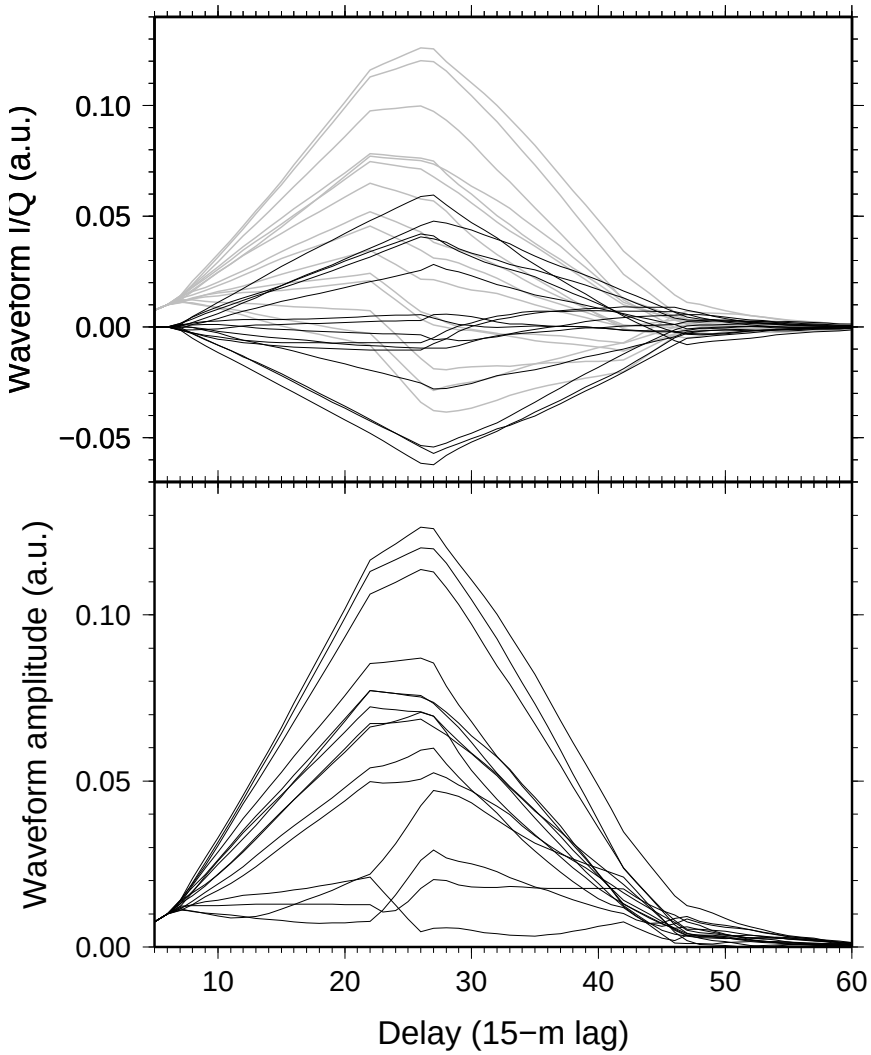

Figure 83.: [Top] Real and imaginary parts of the complex waveforms synthesized using the model in Equation (99). An amplitude of 0.05 has been assigned to the LHCP leakage of the direct signal. The geometric conditions reproduce those in Figure 74, that were obtained with real data. [Bottom] Total amplitude of the waveforms on top. Figure from Cardellach et al. (2012).

5.1.3 LAG-HOLOGRAPHIC ANALYSIS

Radio holography uses coherent properties of the signals propagating through a medium (Igarashi et al., 2000). These properties arise due to the high stability of the GNSS signal and its high sensitivity to layered structures. This approach seeks to obtain the maximum spatial compression of the main ray separately from that of the other rays trajectories. This makes it possible to evaluate the intensity of radio waves at each ray trajectory and to determine the corresponding frequency displacement from a reference ray. A reference wave field (reference ray) is used to reveal the spectra from the total received field.

We choose the direct signal (with no reflection) as a reference field, aiming to see the rest of possible contributing rays present in the data. Once the reference field has been used to counter-rotate the phase of the reflected signal, a spectral analysis is performed. In GNSS radio-occultation applications, the holography is applied at the peak of the received waveform solely (because this is the only data provided by standard and radio-occultation receivers). We here present a new holographic observable that uses each of the lags of the received waveform. The generation of the lag-hologram follows the steps below:

- Time series of N (typically we will use 128) complex (I/Q) waveforms at 1 second sampling obtained from the front-end of the receiver connected to the horizon-looking antenna are taken: $w_r(\tau_w, t)$.
- The phases of each lag τ_w of these waveforms are then counter-rotated by the phase of the direct signal. The direct signal is here defined as the peak of the waveform (lag 22) obtained by the front-end connected to the zenith-looking antenna (w_d). Then: $w_r(\tau_w, t)\ e^{-i\ \phi_d(22,t)}$.
- A Fourier analysis (by FFT) is conducted independently on the time series of each lag to obtain what we refer as **lag-hologram**:

$$\mathcal{W}(\tau_w, f_I) = \mathcal{F}\{w_r(\tau_w, t)\ e^{-i\ \phi_d(22,t)}\} \tag{100}$$

- Since the geometric parameter that changes with time (and thus forces the potential interference to change) is the elevation angle, it is more practical to express the frequency in terms of elevation rate (oscillation cycles/degree-elevation) rather than Hz (oscillation cycles/second). The conversion between them is given by

$$f_I\left[\frac{cycle}{deg-el}\right] = \frac{f_I[Hz]}{\frac{d\varepsilon}{dt}[deg-el/s]} = \frac{f_I[Hz]}{\frac{d\varepsilon}{dt}[rad/s]}\frac{2\pi}{360} \tag{101}$$

- Finally, each lag τ_w of the lag-hologram is normalized (independently to the other lags):

$$\overline{\mathcal{W}}(\tau_w, f_I) = \frac{1}{\sum_k \|\mathcal{W}(\tau_w, f_{I,k})\|}\mathcal{W}(\tau_w, f_I) \tag{102}$$

Another possible normalization would have been a single factor for the entire lag-hologram. We have chosen the lag normalization to give more relative power to the features at the end of the waveform, on those lags of the waveform where the overall power is weak, unmasking frequency contributions that otherwise would be too low

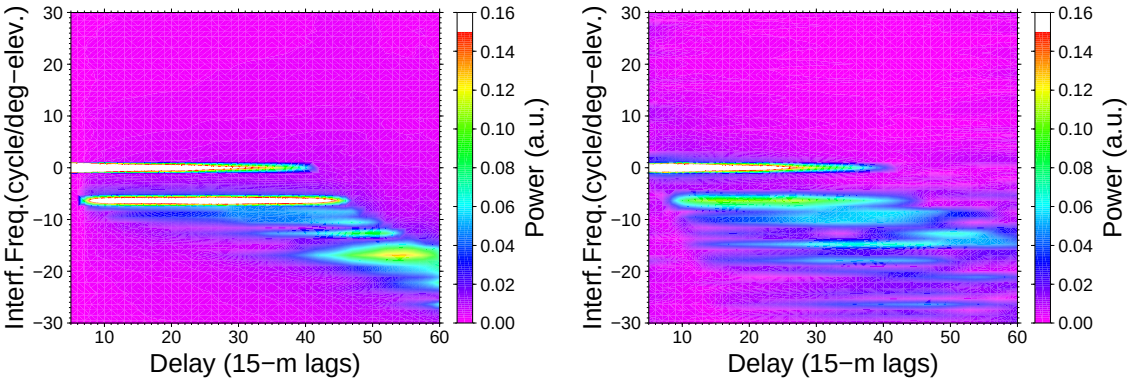

Figure 84.: [Left] Lag-hologram of a series of 128 synthesized complex waveform around $\sim 45°$ elevation. [Right] Lag-hologram for a time series of $N = 128$ 1-second measured complex waveforms under the same geometry as on the left panel. The zero-frequency corresponds to the reference ray, the direct one. According to Equation (104), frequencies more negatives than -5.8 cycle/deg-el correspond to scattering off reflecting-elements below the snow-air interface.

compared to the values around the lag-hologram's peak power. The disadvantage of the lag normalization is that weaker frequencies in powerful lags might also become masked. An example of the effect produced by both types of normalization is shown in Figure 103 from Section 5.2.4.1.

The lag-hologram resulting of a series of 128 synthetic waveforms which include the ones presented in the examples above (Figure 83) is shown in the left panel in Figure 84. The frequency components are given in cycle per elevation degree (see Equations (65) and (101)). The lag-hologram clearly shows a discrete set of interference frequency *bands*, rather than a continuous or broad spectra. The band-structure is clearly odd, indicating that the frequency components are phasor-rotations rather than amplitude modulations (which would generate symmetric positive and negative bands). The zero-frequency corresponds to the direct signal, while ~ -5.8 cycle/deg corresponds to the theoretical interferometric frequency of a reflection off the snow surface ($H_0 = 46$ m and $\varepsilon = 45°$):

$$f_I^{surf}[Hz] = \frac{-1}{\lambda}\frac{d\rho_0}{dt} = \frac{-2H_0}{\lambda}\cos(\varepsilon)\frac{d\varepsilon}{dt} \quad (103)$$

$$f_I^{surf}[cycle/deg - el] = \frac{-2H_0}{\lambda}\cos(\varepsilon)\frac{2\pi}{360} \quad (104)$$

The right panel in Figure 84 displays the lag-hologram generated from real observations under the same conditions. Any reflection off planar-elements above the snow surface would correspond to frequencies computed with H_M smaller than H_0, thus frequencies slower (less negative) than f_I^{surf}. Figure 85 compiles the first negative peak of the lag-holograms observed during December 16 2009, which clearly follow Equation (104). Therefore, it seems that the main bulge of frequency contributions generally captured by the lag-holograms, which are faster (more negative) than f_I^{surf}, might come either from depths below the snow external surface, or from reflectors which do not follow Equation (66). Such reflectors could be tilted reflecting surfaces located above the snow, but at some horizontal distances. In previous Figure 27, the environment of the observation tower was displayed. The Concordia Station buildings are at $\sim$ 800 m dis-

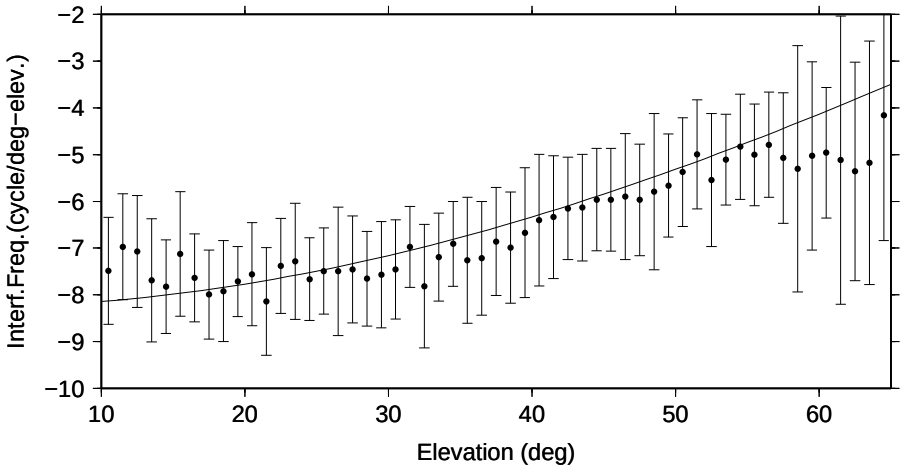

Figure 85.: Averaged location of the first negative peak in the lag-holograms collected during December 16, 2009. The solid line is the theoretical interferometric frequency corresponding to a reflection off the snow-air interface, f_I^{surf} in Equation (104). The dispersion (error-bars) are consistent with the frequency resolution of the lag-hologram, given by the length of the time series (128 seconds) and Equation (101): with $d\varepsilon/dt$ in the range of values between $0.003 - 0.008^\circ/\mathrm{s}$, the frequency resolution lies between 1.0-2.6 $cycle/deg - el$. Frequencies more negatives must come from snow sub-surface reflections. Figure from Cardellach et al. (2012).

tance from the tower, in the direction opposite to the main beam of the antenna. These distances are too long to be captured within our waveform (42 lags after the direct signal, which is 630 m range delay with respect to the reception of the direct radio-link). A small shelter is closer to our antennas, at $\sim$ 100 m in the back-lobe direction. The fact that it is in the blind area of the antenna, together with its small size (which hinders the generation of continuous multipath, from any incidence angle), makes it difficult to believe it might generate the strong and continuous patterns observed in the data.

Thus, our hypothesis is that the presence of multiple reflections within the dry snow sub-structural layers are responsible of the interferometric patterns found in the data.

5.1.3.1 *Snow depth retrieval and spatial resolution of the lag-hologram*

From Section 5.1.2.1 we know that because the incidence angle of the observation constantly evolves in time, the delay between the direct and reflected signals also changes in time, producing then an interferometric frequency (with respect to the direct signal) that can be obtained from Equations (65) and (101), where ρ_M is now the delay of the layer-reflected signal with respect to the direct one. The interferometric frequencies corresponding to each snow layer, computed from the MRSR model (having the snow density profile as a unique input), are displayed in Figure 86. With this conversion method, we can transform the frequency-axis of the lag-hologram into a depth-axis, and thus the spectral stripes relate to the snow layers that reflect signal towards the receiver.

The vertical resolution of the identified layers is mainly given by the length of the time series used to generate the spectral analysis (FFT resolution). Other secondary factors are the geometry (see different slopes in Figure 86 as function of the elevation angle due to

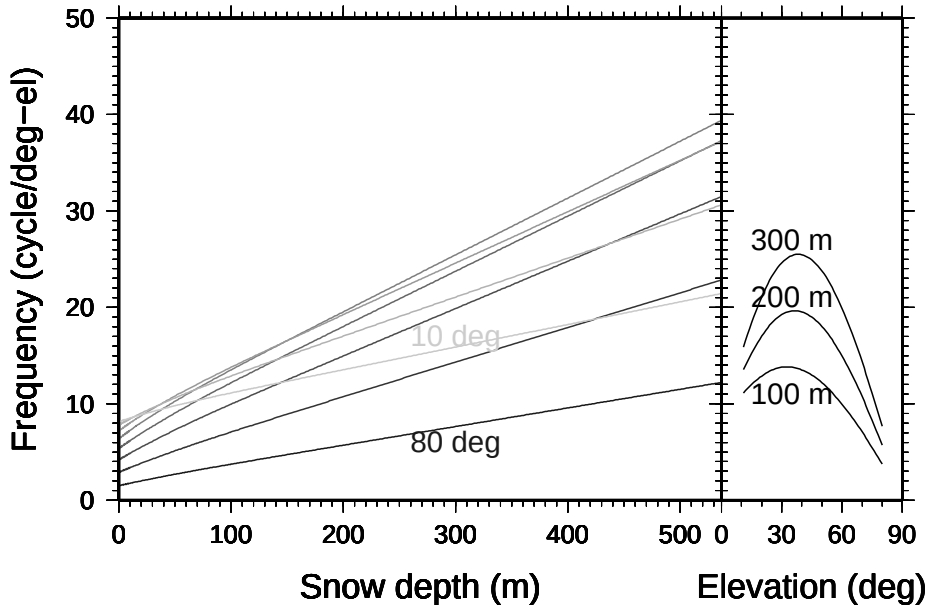

Figure 86.: A ray propagating into the snow, down to the x-meter depth layer, reflected at that layer, and propagated upward to reach the receiver, arrives with a y-frequency with respect to the direct signal (Equations (65) and (101)). For a given elevation rate of variation, it depends on the elevation angle of observation: gray hues, from 10° to 80° elevation, in steps of 10°, lighter to darker respectively. The dependency on the elevation angle is also shown on the right frame, where the interferometric frequency in the signals reflected by layers 100, 200, and 300 m deep are plotted as function of the elevation angle. Values from the MRSR model assuming the snow density profile given in Figure 134. Figure from Cardellach et al. (2012).

different elevation rates). For 128 samples of 1-sec integration, the approximate vertical resolution ranges between 5 and 15 meter. This could be improved by increasing the length of the time series. However, the impact of significant geometric changes suffered by the observation along the –longer– event might worsen the results (as later analysis will show in Section 5.2.2.3).

The horizontal resolution of the measurement in the direction perpendicular to the line-of-sight is of the order of 5-10 meter, and it is given by the first Fresnel zone. The resolution along the line-of-sight direction is given by the displacements of the specular points in deep layers (related to D_k in Figure 77 and Equation (80)). Assuming that the captured reflections might occur down to $\sim$300 m depth, the resolution along the line-of-sight is of the order of $\sim$350 m. Note that line-of-sight resolution worsens with depth.

5.1.3.2 *Depth sensitivity to inaccuracies in the snow density profile*

We have seen that each frequency stripe in the lag-hologram is assigned to a given depth of the reflecting layer by means of the MRSR model with a snow density profile. This section tries to understand how sensitive the vertical location of the layer is to inaccuracies of this profile. To assess this question, a set of synthetic runs have been performed. We employ a realistic but smooth analytic expression obtained by means of an exponential fit to the *ground truth* discrete density profile:

$$\rho_s = 0.92 - 0.6e^{-\left(\frac{\delta_s}{60} + \frac{\delta_s^2}{30000}\right)} \tag{105}$$

A set of perturbations to this smooth profile have been added. A perturbation is here a Gaussian function added to the smooth profile, of relatively large intensity (0.1 gr/cm^3, representing more than 10 % of the highest density) and vertical size ($\sim$20 meter half-width), and variable depth-location. It is illustrated in the top panel in Figure 87. For each of these perturbations, the model has been run to find the relationship between interferometric frequency and snow depth. This has been done for a geometry around 45° elevation angle. Different geometries would yield different results, but of similar order of magnitude.

The error introduced by these uncertainties is given in the bottom panel in Figure 87. It is clear that even large uncertainties such as the Gaussian perturbations added in the smooth profile introduce errors below 2.5 %. In 5 out of the 6 cases the error is lower than 1%.

5.1.3.3 *Discretization effects in the lag-hologram*

The model relies on a discretized set of layers, given by the discrete sampling of the density profile. This may induce *fake* interfaces, just because the permittivity is not continuously sampled:

According to Equations (85) and (86), the limit in which the permittivity ϵ_{ds} is smooth and continuous would result in no internally-reflected signal. The fact that our permittivity is given in a discrete set of snow depths artificially introduce jumps in ϵ_{ds}, which might produce artificial interferences wrongly interpreted as internal reflections.

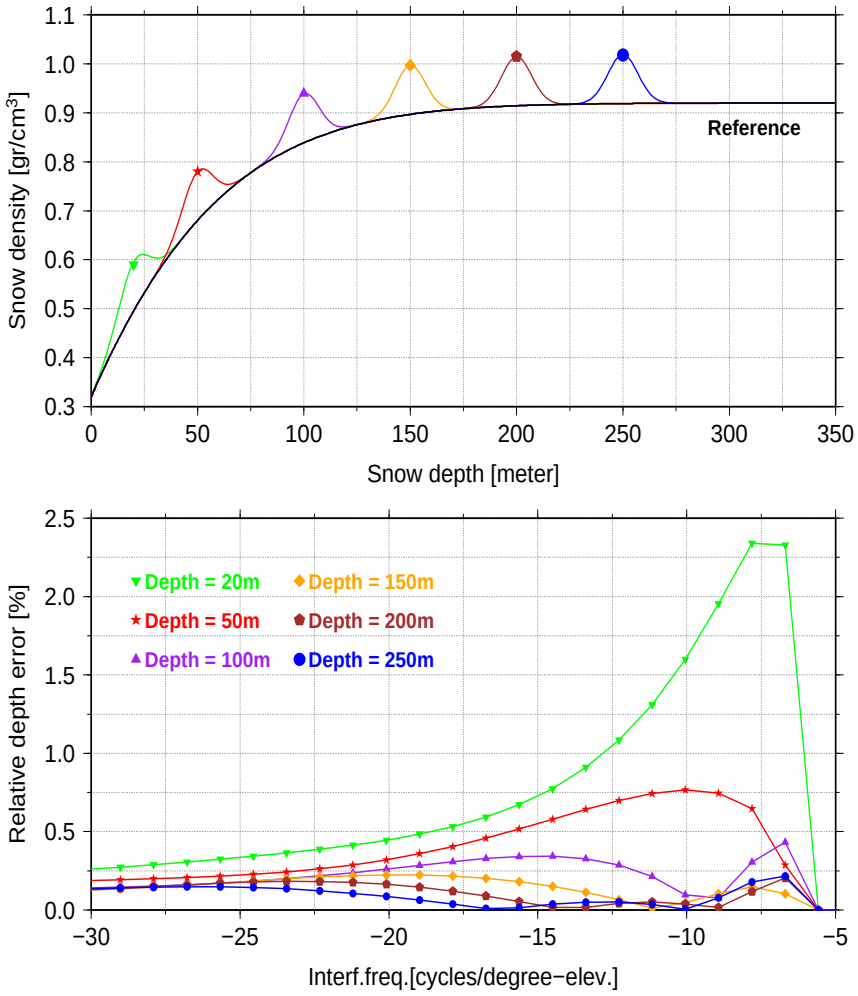

Figure 87.: [Top] A smooth analytical expression of the snow density is used to estimate a generic relationship between interferometric frequency and snow depth. The smooth profile is then perturbed by Gaussian bulks, of large intensity (>10% of the highest density), ∼20 meter vertical half-size, and located at different depths. [Bottom] The link between interferometric frequency and depth of the snow reflecting layer is computed assuming a given density profile. This panel shows the error in the snow depth location introduced by each Gaussian perturbation, with respect to the depths obtained with the non-perturbed reference profile. Figure from Cardellach et al. (2012).

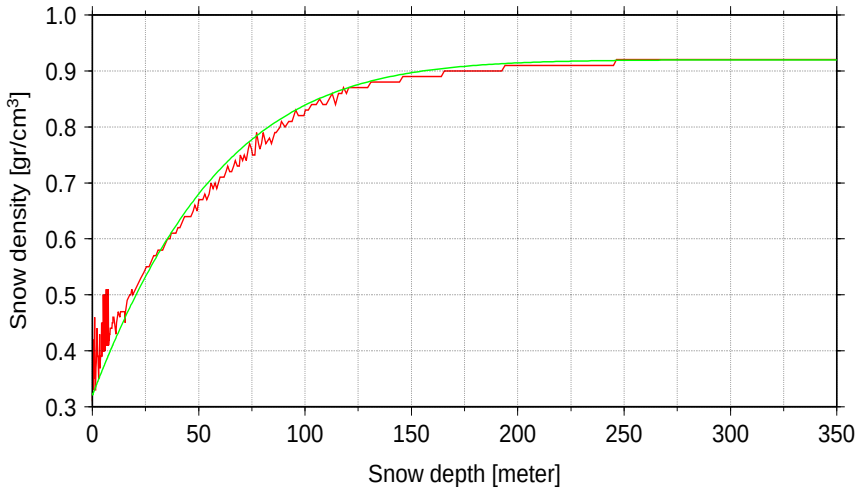

Figure 88.: Ground truth density profile, in red, together with the smoothed analytical expression (exponential fit), in green, used to check the effects of discontinuous sampling of the density into the MRSR model.

In order to check how sensitive is our approach to the level of discretization given by the density profile, we have run two examples (see Figure 88):

- 1-cm discrete sampling: the model has been run using the analytical expression of the snow density in Equation (105) at 1-cm discrete layers, around 50° elevation angle, in 256-0.006° steps (from surface to 200 meter depth solely).
- 1-m discrete sampling: same as above but using 1 meter resolution.

The amplitude of the reflected signals coming from each of the 1-cm and 1-m discrete layers are shown in Figure 89, together with the delay of a reflection off each of these layers. The figure shows that the only significant contribution comes from the external interface (air-snow), and the amplitudes quickly drop afterward (quicker in 1cm-resolution than 1m-resolution). Both discretization levels produce the same delays (delay computation not affected by discretization).

The resulting lag-holograms are displayed in Figure 90. The only clear reflection when discretizing at 1-cm level comes from the external interface, at ∼-5 cycle/deg-elevation. The 1-meter discretization introduce some artificious reflection bands at the end of the trailing edge.

The resolution of the *ground truth* density profile given by IFAC stays below or around 1 meter during the first 90 meters, and ∼1.5 meters afterwards. Therefore, the level of artificious reflection bands should be weak and mostly affecting the end of the tail of the log-holograms.

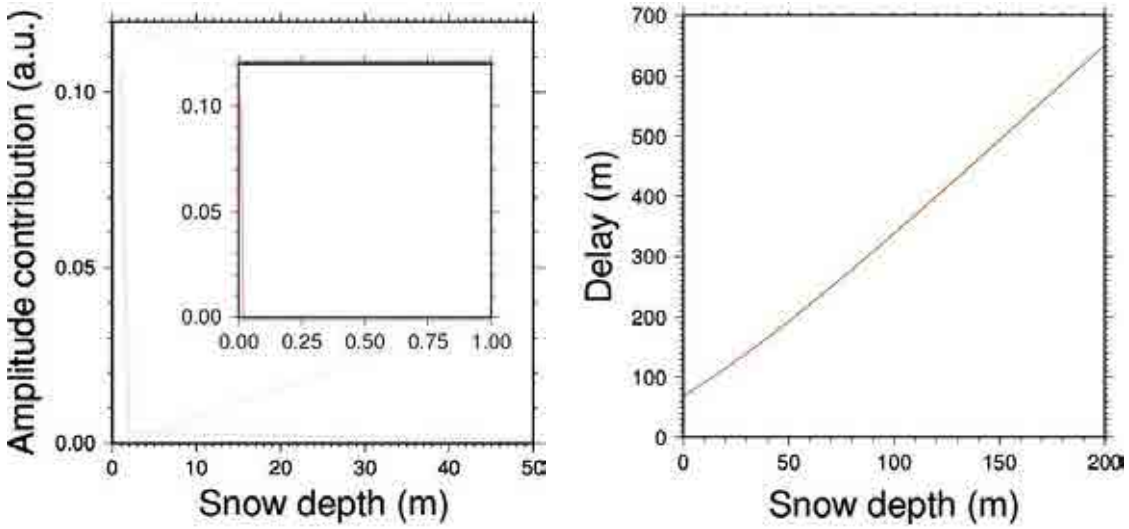

Figure 89.: Amplitude (left) and delays (right) of internal reflections in a smooth medium (Equation (105) and Figure 88), sampling at 1-cm layer resolution (red) and 1-meter (green).

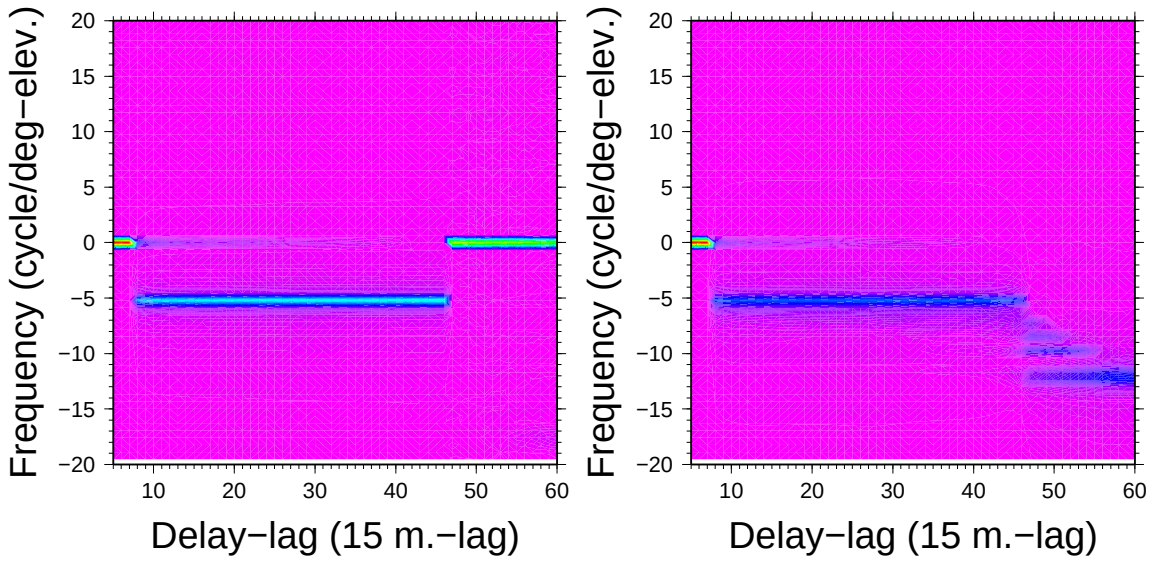

Figure 90.: Lag-holograms of the discretization-exercise: [Left] 1-cm layer resolution on a smooth medium (Equation (105) and Figure 88); [Right] same at 1 meter discretization.

5.1.4 ALTERNATIVE: THREE-REFLECTION MODEL

Based on the Single-reflection model, we have also implemented a model in which 3 reflections occur within a layer. That is, a reflection off the bottom of the layer; a reflection off the top of the layer; and finally a last reflection off the bottom again. With this odd-number of reflections the resulting polarization is LHCP (as in single-reflection). An sketch is provided in Figure 91. Because of the low power expected from these sort of reflections, of the order of $\Re^3_{cross}$, we have not implemented a full model to build complex waveforms based on these 3-reflection events, but we just use the model to have an estimation of the interferometric frequency that such an event would introduce.

The delay of a ray reflecting 3 times within the *i*-layer, would just be (compare with Equation (79)):

$$\rho_i = \rho_0 + \sum_{k=1}^{k=i-1} 2n_k \frac{H_k}{\cos(\theta_k)} + 4n_i \frac{H_i}{\cos(\theta_i)} - \left(\left(\sum_{k=1}^{k=i-1} D_k \right) + 2D_i \right) \sin(\theta_0) \tag{106}$$

The result of playing with this model, assuming triple-reflections within layer-areas in which the real density profile seems to facilitate these sort of events are:

- Triple-reflection within a layer 3-meter thick located at 74 meter depth arrives with a delay of the order of ∼500 meter (change with incidence angle). Delays of this order of magnitude came from single-reflections at layers in the range of ∼100 to ∼200 meter depth.
- The interferometric frequency is not necessary higher than single-reflection events (it changes with incidence angle), but of the same order of magnitude.

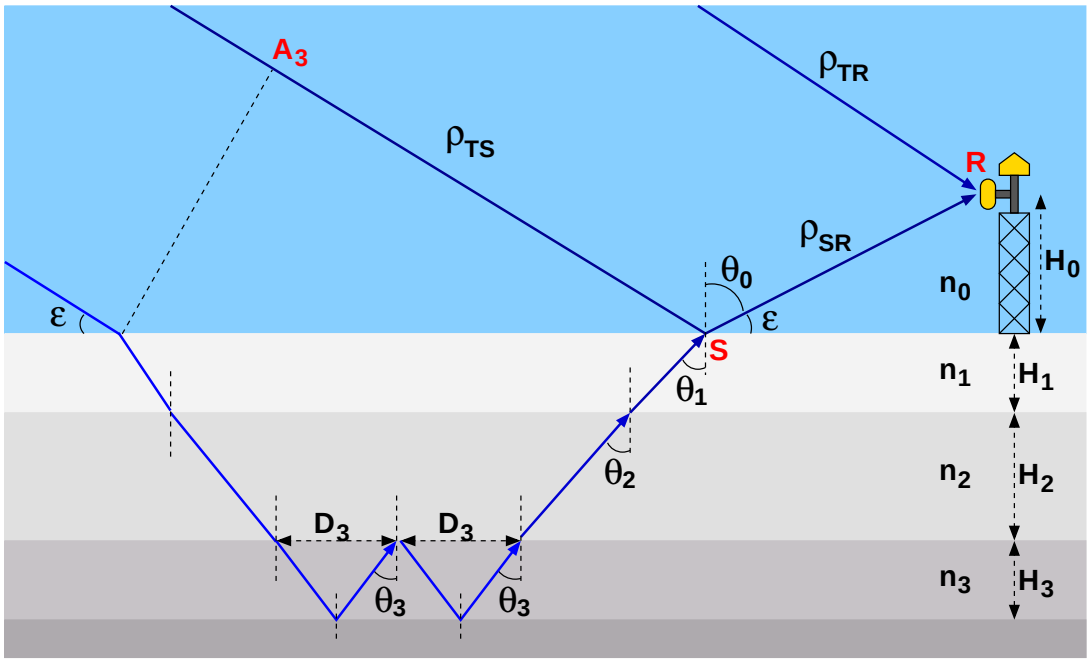

Figure 91.: Sketch of the delays induced by a 3-reflections event within a certain layer.

As it will be explained in the following sections, the features in real data do not necessarily require the three-reflection model to be understood. This, together with the very low power with which they would reach the receiver, make us disregard this model.

5.2 EXPERIMENTAL RESULTS

5.2.1 REPEATABILITY AND ROBUSTNESS OF THE SIGNALS

The lag-holograms computed from the collected waveforms present very high repeatability, day after day. This is displayed in Figure 92, where the lag-holograms of observations by the same GPS satellite and occurring at the same geometric conditions as the example given in Figure 84 are presented for the next four subsequent days (17 to 20 December 2009, PRN 13). The features are almost identical every day. Similar interferences and their repeatability are found in all observations during the campaign (every GPS satellite, at every azimuth and elevation).

In order to check which features of the lag-hologram consistently persist, several averaging analysis have been conducted. The features that do not persist (i.e. evolve and

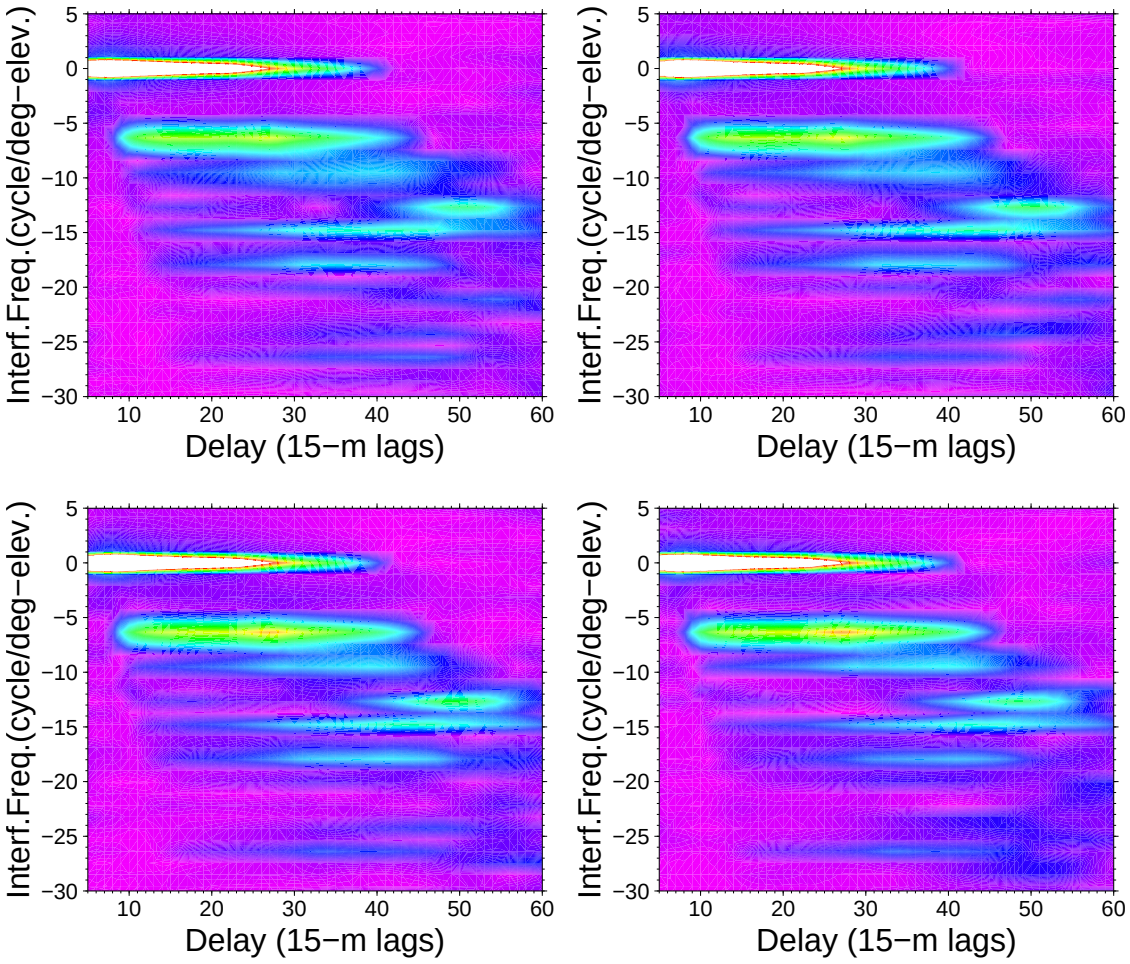

Figure 92.: Repeatability of the lag-holograms for different days: Lag-holograms obtained with the same time series of observations (PRN 13, and elevation angles) as in Figure 84, but for the next four subsequent days: 17 to 20 December 2009 (sequentially from left to right, and top to bottom). Note that the plots zoom into the range of frequencies of interest [-30,5], whereas Figure 84 displayed the range [-30,30]. Color scale given in Figure 84.

change) along the averaging series will tend to fade away, while those that stay will emerge above the faded background.

The goal is twofold: (1) to fade away those other features of the data which are not consistently repeated (noise, atmospheric and instrumental induced features); and (2) to identify the geometric and experimental parameters which essentially drive the interferometric signal.

If the model we developed were accurate, we would expect the elevation angle of observation, together with the elevation rate, to be the main drivers of the lag-hologram (changing elevation and elevation rate would result in varying lag-holograms). If the snow layers were not homogeneous across the observation area, differences would be also detected for different azimuths (or GPS satellites–PRN).

The average analysis is split in four types:

- **PRN:** lag-holograms corresponding to the same PRN are averaged, each day independently. Each average lag-hologram contains a wide range of elevation angles of observation and elevation rates. Each PRN covers a given fraction of the azimuth. Daily differences might be related to changes in the extension of the satellite's ground-track (i.e., extension of its elevation and elevation-rate parameters).

- **Elevation:** lag-holograms corresponding to the same elevation angle ($\pm 2.5^\circ$, elevation grid of 5° cells) have been averaged, each day independently. The averaged values contain a wide range of satellites and elevation rates. Daily differences might be related to different number of PRNs being present at that elevation-cell (with different elevation rates).

- **Elevation Rate:** lag-holograms corresponding to the same elevation rate ($\pm 0.0005^\circ/s$, or elevation rate grid of $0.001^\circ/s$ cells) have been averaged, each day independently. The averaged values contain a wide range of satellites and elevation angles. Daily differences might be related to different number of PRNs being present at that elevation rate cell (with different elevation angles).

- **Elevation and Elevation Rate:** lag-holograms corresponding to the same elevation angle and rate (grid of $5^\circ \times 0.001^\circ/s$ cells) have been averaged, each day independently. The averaged values contain a wide range of satellites, and daily differences might be related to different number of PRNs being present at that elevation/elevation-rate cell.

In this section, we will focus on the fourth type of analysis, which better summarizes the general behavior. The results obtained with the other types are compiled in Appendix G.

It is thus relevant to begin this analysis with a picture of the evolution of the observation scenario, day after day. Figure 93 contains the PRN tracks as function of their elevation and elevation-rate, in daily shots, and Figure 94 the histogram of number of observations within every elevation/elevation-rate cell, in daily shots. Only the dates with maximum number of observations have been considered (December 16 to 20), plus a day with a low number of observations (December 21) for comparison.

For each day (between 16th and 21st December 2009), all the lag-hologram observations laying within 5° elevation angle and 0.001°/s elevation rate cells have been aver-

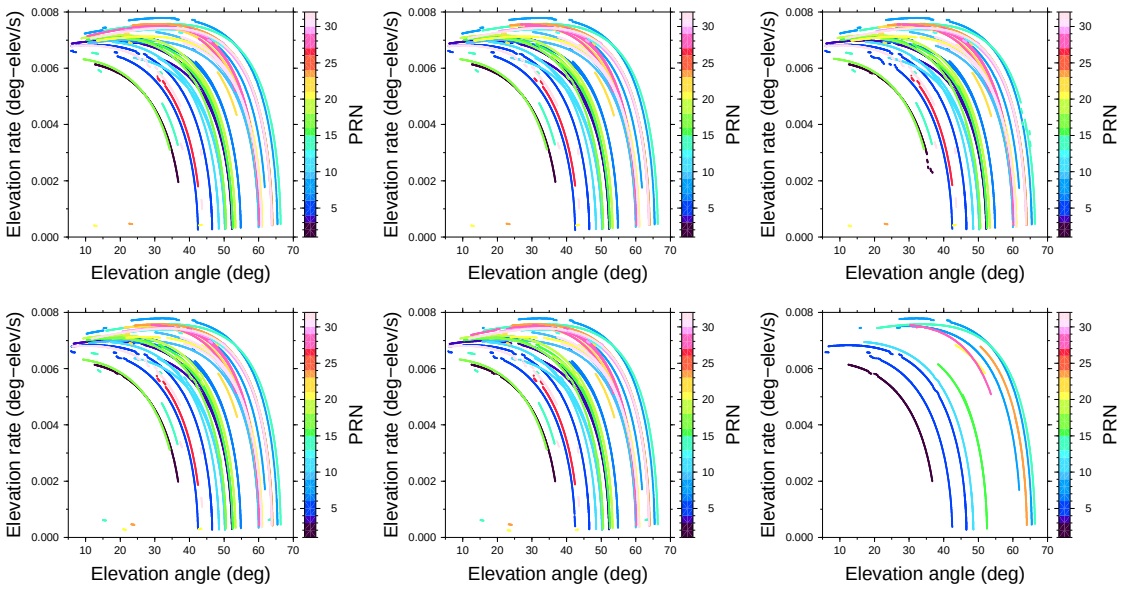

Figure 93.: Daily PRN tracks as function of the elevation angle and elevation rate, for each day between December 16 and 21, 2009. The color scale states for PRN number, same color scale used every day.

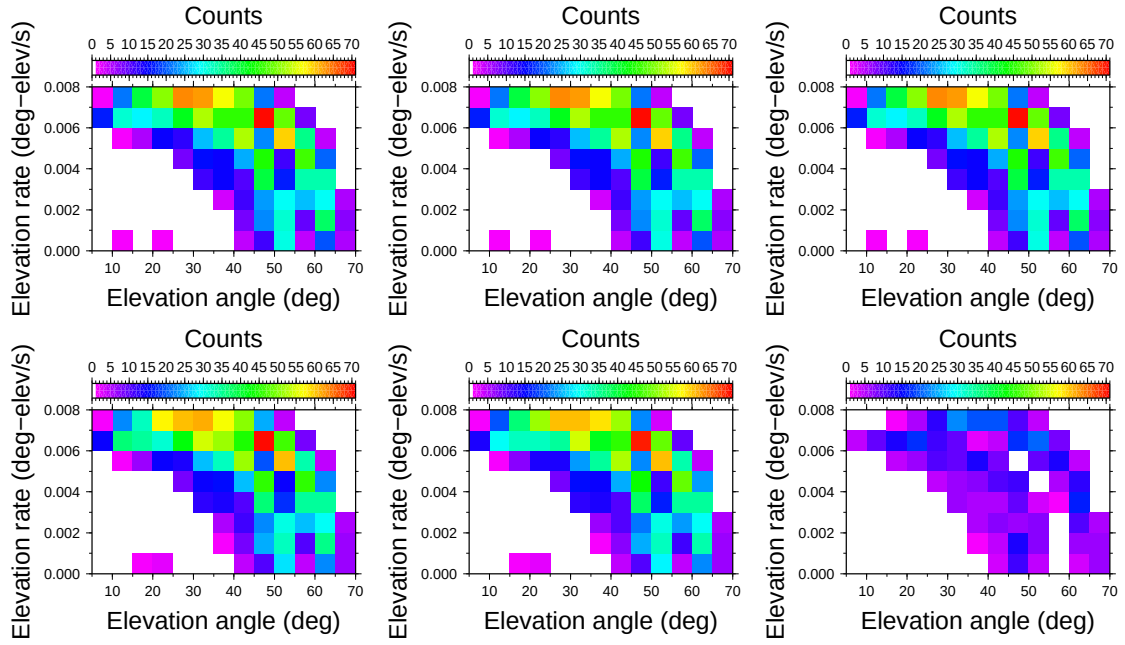

Figure 94.: Daily number of observations within every elevation/elevation-rate cell, for each day between December 16 and 21, 2009. The color scale states for number of counts, same color scale used every day. 1-count is an individual lag-hologram.

Elevation	Elevation-rate
12.5°	0.0075°/s
27.5°	0.0075°/s
47.5°	0.0075°/s
32.5°	0.0055°/s
57.5°	0.0055°/s
47.5°	0.0035°/s
62.5°	0.0035°/s
47.5°	0.0015°/s
62.5°	0.0015°/s

Table 20.: Selected elevation/elevation-rate cells.

aged. Each cell thus contains the variability associated to the width of the cell, plus the diversity of geographic locations of the reflection (different PRNs, azimuths).

Only cells containing more than 20 radio-hologram samples have been considered. These are a total number of 37 to 46 cells (it depends on the day), except for December 21 2009, with just one cell exceeding 20 counts. Because of the large number of cells to compare (among them and day-after-day), we focus on a few ones, which all together are representative of the elevation/elevation-rate space covered by the PRN tracks. The selected cells are listed in Table 20 and displayed in Figure 95.

The results show that a minimum elevation and elevation-rate are required to get a wide variety of persistent fringes from sub-surface contributions (interferometric frequencies mostly under -6 cycles/deg-elev) in the lag-holograms. We could qualitatively set those lower bounds around 30° and 0.006°/s respectively. The explanation of this behavior is given by the relationship between depth's retrieval and these two magnitudes: for a fixed time window of the data-series (128 samples at 1 Hz), the delay $-\rho_i-$ variability that could be measured is directly proportional to elevation (the differential delay of each additional deep layer increases with it) and to elevation-rate along the series, and thus the interferometric frequency and the depth retrieved from it. This effect could be also visualized as how for low angles of elevation or without elevation variation, the incremental delay variation in the reflected signal obtained from deep layer contributions is nearly negligible and no depth can be retrieved by means of the lag-holographic analysis. To obtain such type of behavior from real data is therefore consistent with our hypothesis of multiple sub-surface reflections.

In general, this averaging exercise has shown a very high time repeatability (see an example in Figure 96), resulting in almost identical lag-holograms day after day (except for December 21, when less data/statistics were available). The signatures persist in all PRN-, elevation-, elevation rate- and elevation/elevation-rate averages.

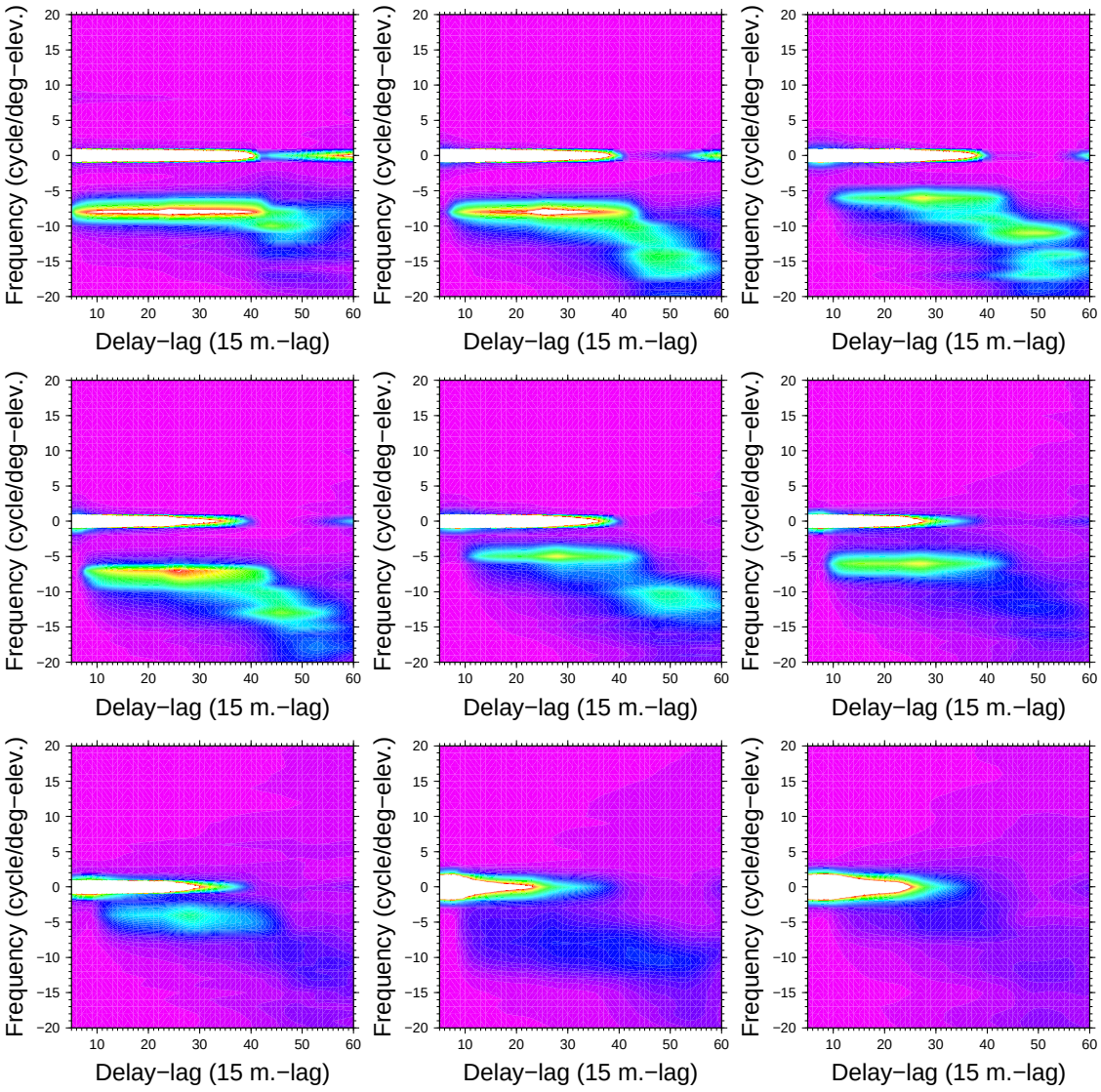

Figure 95.: Elevation/elevation rate-averaged lag-holograms for December 16, 2009. All figures use the same color-scale (arbitrary units). Left to right and top to bottom correspond to the list sorting in Table 20.

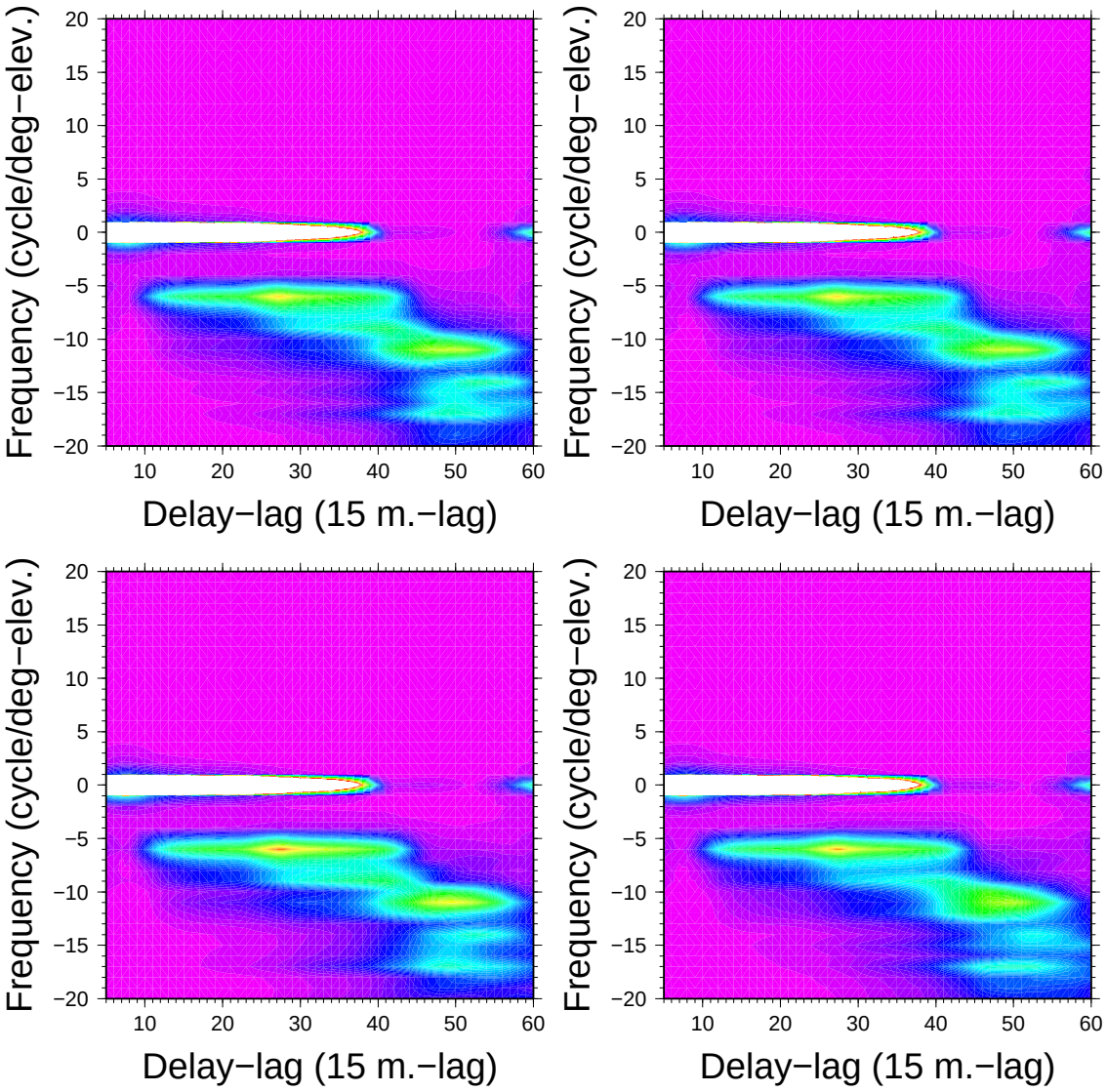

Figure 96.: Repeatability of the elevation/elevation-rate averaged lag-hologram, corresponding to the cell (47.5±2.5°, 0.0075±0.0005°/s), December 17 to 20, 2009 (left to right, top to bottom). All figures use the same color-scale (arbitrary units).

5.2.2 CONSISTENCY WITH THE MODEL

5.2.2.1 *Comparison with the elevation/elevation-rate averages*

Given that the elevation/elevation-rate averaged cells should be better represented by the model (in which both elevation and elevation-rate can be tuned), we first compare the cell-averaged data with runs of the model corresponding to the central parameters of the elevation/elevation-rate cells.

The central values of the cells selected in Table 20 and shown in Figure 95 are thus simulated with the model, and the resulting lag-holograms are displayed in Figure 97. As expected, the model run at the central parameters of the cell do not account for the diversity within the cell, thus producing sharper (less blur and fading) images, of higher frequency resolution. Besides this effect, the main features of the model are present in the averaged data lag-holograms, including the resolution loss experienced at low values of elevation and elevation-rate.

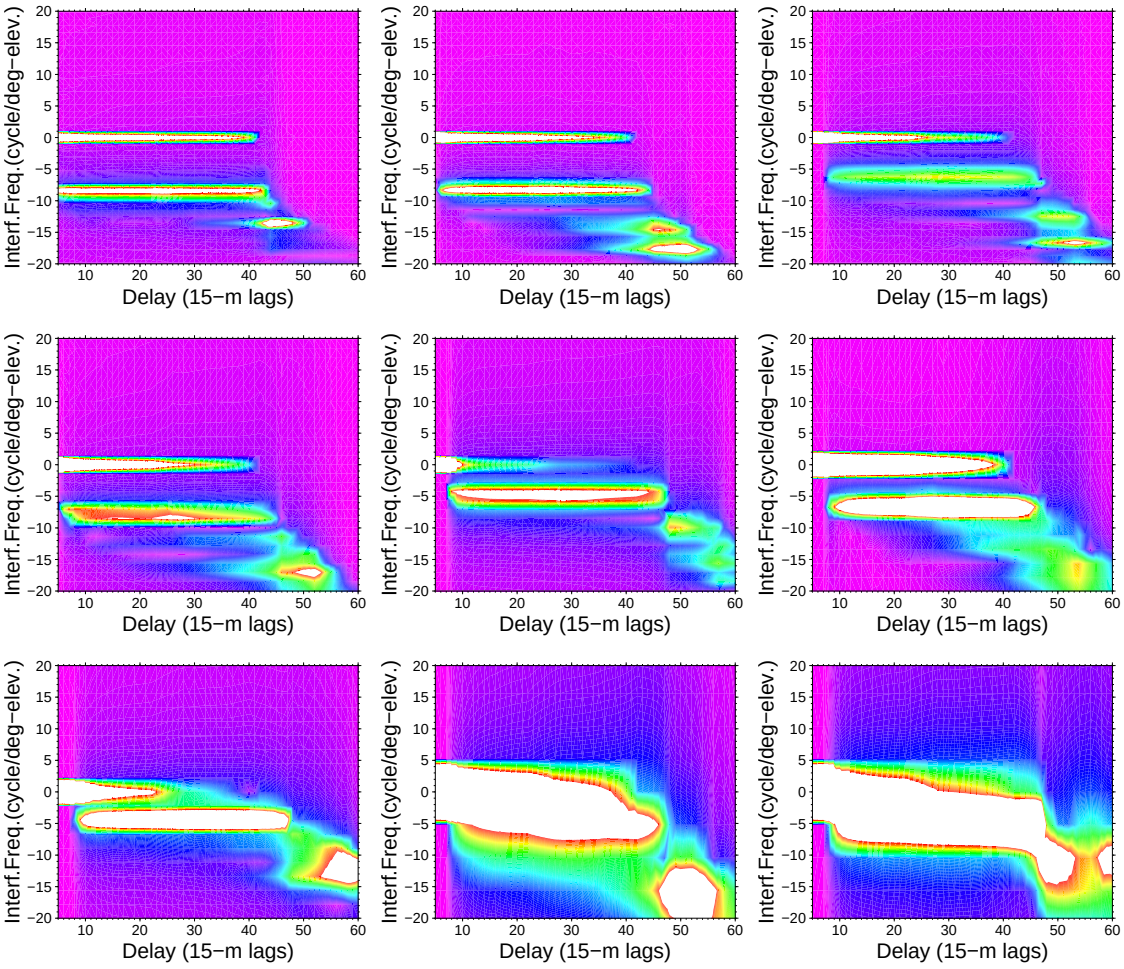

Figure 97.: Elevation/elevation-rate modeled lag-holograms. Color scale given in Figure 84. Left to right and top to bottom correspond to the list sorting in Table 20. Compare with Figure 95.

5.2.2.2 *Comparison with non-averaged lag-holograms*

The consistency with the model has been checked for a wide range of elevation angles of observation. We will consider again PRN13 collected during December 16, 2009 (as the preliminary results shown in Section 5.1.3). 128 1-second samples are used to compute the FFTs. This operation is repeated around elevation angles 15°, 25°, 35°, 45°, 55° and 65° (along the ground track). Figures 98 to 99 display the lag-holograms obtained with real data, as well as the output of the model. Notice that only two cases achieve the minimum elevation and elevation-rate levels (around 30° and 0.006°/s respectively) to get the best performance.

From the results obtained, we can observe that each pair of model/data lag-holograms agree on the approximate location of the few first frequency-bands. A significant difference relies on the impact of the first reflection band (closer to the surface at around -6 cycle/deg-e, depending on the geometry) on the whole lag-hologram. While the real data output shows relatively strong bands between -8 and -12 cycle/deg-e in the lag-delay range 12-44, the model is apparently masking these layer's contributions after the normalization. That would mean that reflections coming from the first 50 meter deep in snow are stronger than expected (comparable to the –air/snow– surface reflection).

Moreover, some high negative frequency components seem to persist in lag-delay areas which are in-consistent with the model. For instance, the bands at ∼-25 and ∼-28 cycle/deg-e visible between lags 30 and 40 would correspond to reflections off very deep layers, reaching the receiver at very long delays. These very long delays should not contribute into these lags, because of the code-delay filtering of the GPS signals. As

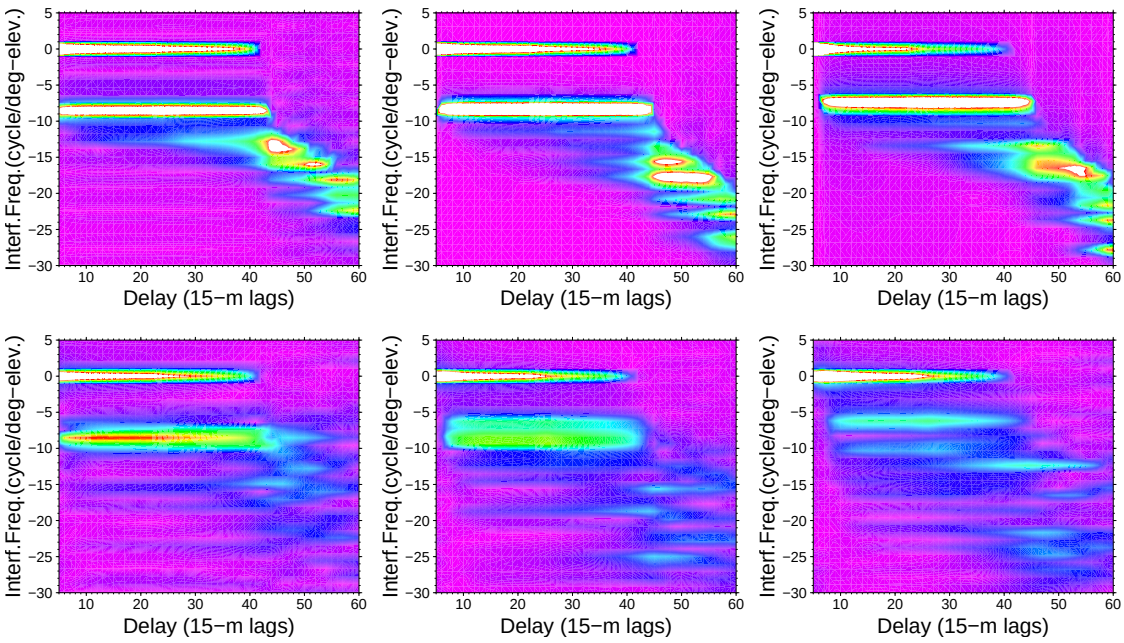

Figure 98.: Individual lag-holograms (Up-model, Down-real data) for PRN13, in FFT windows of 128 1-sec samples, from December 16th. Different elevation angles and elevation-rates are considered: [Left] 15° and 0.0073°/s, [Center] 25° and 0.0075°/s, [Right] 35° and 0.0076°/s. Model and real-data color scales, given in Figure 84.

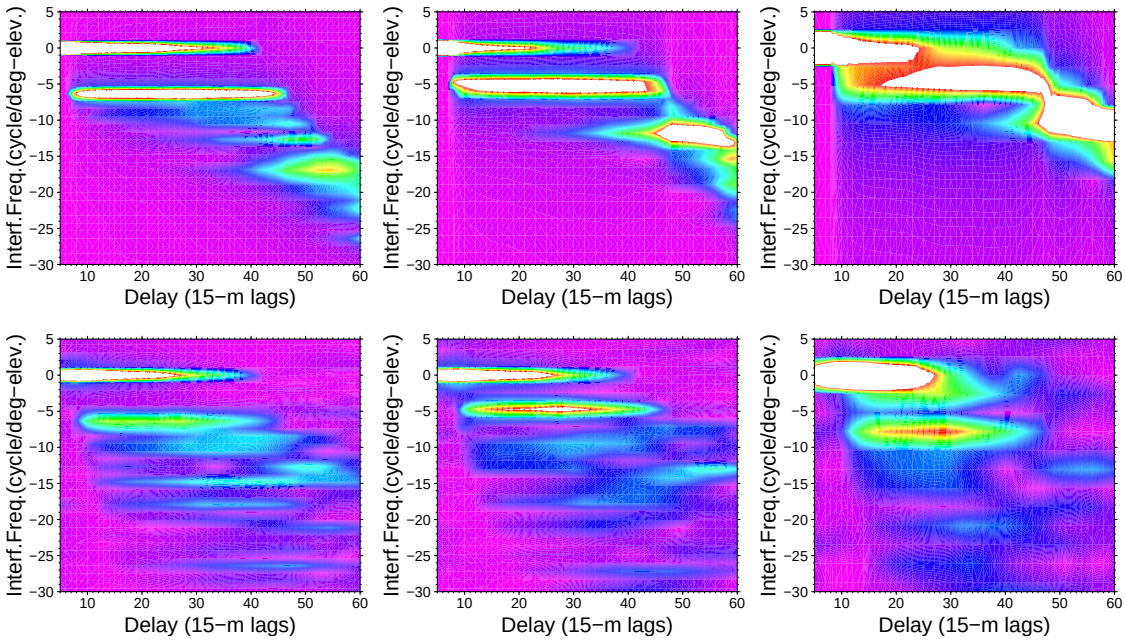

Figure 99.: Individual lag-holograms (Up-model, Down-real data) for PRN13, in FFT windows of 128 1-sec samples, from December 16th. Different elevation angles and elevation-rates are considered: [Left] 45° and 0.0074°/s, [Center] 55° and 0.0066°/s, [Right] 65° and 0.003°/s. Model and real-data color scales, given in Figure 84.

explained in Section 5.1.4, the triple-reflection model neither explains these bands (tripe-reflection model does not predict so much high interferometric frequencies, and it does predict very long delays, inconsistent with the lag-location of these bands). Therefore, other reasons should be investigated. However, note that these effects decrease after averaging the results from several observations (as shown in Figures 95 and 96).

5.2.2.3 *Lag-holograms with higher resolution*

In addition to the considered FFT-lengths of 128 samples from the previous lag-holographic analysis, longer windows of data-series have been also tested. Due to basic Fourier-transform properties, for the same geometric conditions and sampling rate, the number of samples is directly proportional to the frequency resolution (and thus depth resolution). The results obtained under the same geometric conditions as the example given in Figure 84 are displayed in Figure 100. We can observe how, in spite of the resolution improvement, the frequency bands found in the data show poor agreement with the models. The impact of significant geometric changes suffered by the observation along the –longer– event might worsen the results, thus increasing the inconsistencies found in previous Section 5.2.2.2.

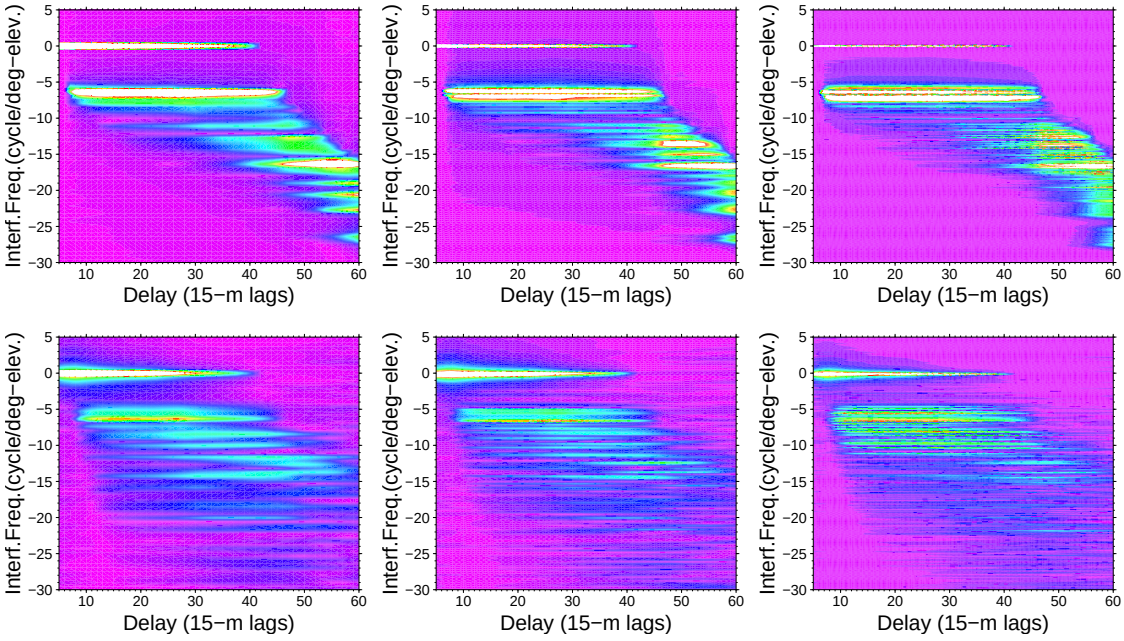

Figure 100.: Lag-holograms (Up-model, Down-real data) for PRN13 at around 45° of elevation (0.0074°/s of elevation-rate) from December 16th. Different FFT windows of 1-sec samples are considered: [Left] 256 samples, [Center] 512 samples and [Right] 1024 samples. Color-scale in arbitrary units.

5.2.3 APPLICATION: DEPTH OF THE CONTRIBUTING LAYERS

As mentioned in the introductory section, the main scientific question we seek to answer is whether the GNSS-R techniques have potential to identify the depth of the snow layers from which the signal is mostly reflected. To do so and as an intermediate step, we first integrate the lag-holograms along the lag-axis, to obtain the total spectral power as a function of the snow depth. An example is given in Figure 101. The profile shows four clear echoes located at ∼5, 90, 130, and 240 meter depth. The figure also displays the integrated spectra obtained with the MRSR model and the given density profile. Some– but not all–of the reflecting layers agree with the data. The discrepancies could be due to inaccuracies in the density profile assumed by the model, or by locally tilted interfaces (not considered in this initial model).

Some snow layers appear consistently in many of the lag-holograms as reflecting elements. Those are identified in Table 21. However, in spite of the high temporal repeatability found in each GPS satellite data, the layers identified by different satellites are not always coincident, that is, the results present high temporal repeatability, but poor geographic consistency. This could be due to a diversity of causes, among them possible inhomogeneities in the snow across the scanned area, ∼500 meter long; and the limited capability of the simple MRSR model to explain all the features in the data. To account for tilted layers in the sub-surface structure could be a possible way to improve the forward model.

Depth [m]	10	70	130	240

Table 21.: List of snow sub-structural layers that reflect signal towards the receiver producing interference patterns, as consistently appear in most of the lag-holograms at ∼45° elevation angle of observation.

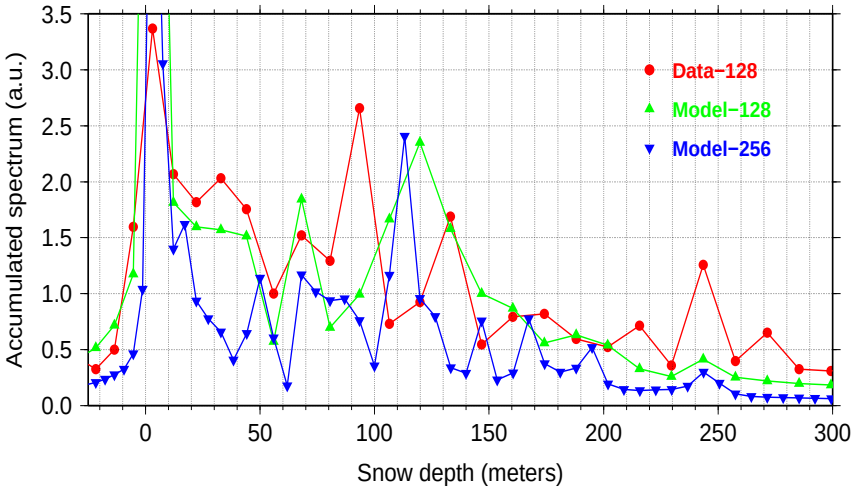

Figure 101.: (Circles:) The frequencies in the lag-hologram shown at the right panel in Figure 84 have been converted into snow depth using Equations (65) and (101). This figure shows the sum of all its lag (integration of the lag-hologram along the lag-axis). Observation corresponding to PRN13, 16 December 2009, at 45° elevation. (Triangles:) Integrated spectral power obtained with the MRSR model run in 128-steps, the geometry of which is identical to the geometry in the 128 samples used to generate the data in circles. (Inverted triangles:) Same as the triangles, but using a series of 256 synthetic observations to improve the frequency resolution. Figure from Cardellach et al. (2012).

5.2.4 TOTAL INVERSION

The analysis presented in Section 5.1 relies on the knowledge of the profile of permittivity layers. That is, the relationship to link frequency stripes with depth of the layers is based on a given profile of snow densities.

The possibility to perform direct inversion of the lag-holograms to retrieve the snow density profiles is here investigated.

5.2.4.1 *Model sensitivity*

The first step to asses the feasibility of total inversion consist in analyzing the sensitivity of the model. Most of the inversion approaches rely on a cost function to be minimized. This cost function usually takes the squared differences between the data and the model, evaluated at different unknown-parameters. To gauge the cost function appropriately, the sum of the squared differences are weighted with the inverse of the data noise. In this first simple sensitivity exercise we only take into account the model, that is, the squared differences scan the model space to compare with a *synthetic truth* model (particular case of the model). Each lag-hologram $\mathcal{W}$ within a study window of $K \times J$ components (τ_w from 5 to 60 lags and f_I from -20 to 20 cycles/deg-elevation) is arranged as a 1-D array of $N = K \times J$ elements:

$$Y_{\mathcal{W}} = \begin{bmatrix} \mathcal{W}(\tau_{w1}, f_{I1}) \\ \mathcal{W}(\tau_{w1}, f_{I2}) \\ \vdots \\ \mathcal{W}(\tau_{w1}, f_{IJ}) \\ \mathcal{W}(\tau_{w2}, f_{I1}) \\ \mathcal{W}(\tau_{w2}, f_{I2}) \\ \vdots \\ \mathcal{W}(\tau_{wK}, f_{IJ}) \end{bmatrix} \tag{107}$$

Since we are interested in evaluating how sensitive the model is around a particular perturbation case $Y_{\mathcal{W}}^{p_{ref}}$, compared to a set of other model perturbations $Y_{\mathcal{W}}^{p}$, the cost function to evaluate becomes:

$$S_C(p; p_{ref}) = \sum_{i}^{N} (Y_{\mathcal{W}}^{p}[i] - Y_{\mathcal{W}}^{p_{ref}}[i])^2 \tag{108}$$

As explained before, the lag-by-lag normalization permits the weak signals at the end of the trailing edge to emerge, but it masks the secondary signals in the central lags. A normalization using the total lag-hologram power within the study window, masks the weak signals in the trailing edge but allows to emerge the secondary contributions in the central lags. The sensitivity of both normalization approaches has been tested.

The density profile considered for this sensitivity profile is the smooth analytical expression from Equation (105), sampled at 1 meter layers. The density perturbations considered are $\Delta\rho_s = 0.05$ gr/cm^3 added at one particular layer (depth), as illustrated in Figure 102. Therefore, the cost function value $S_C(12; 20)$ evaluates the overall difference between the lag-hologram resulting from a profile with a 0.05 gr/cm^3 perturbation

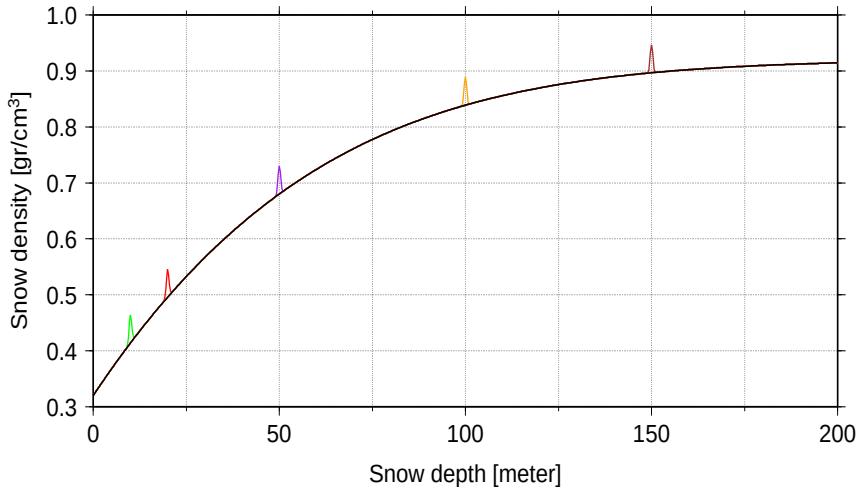

Figure 102.: Examples of density profiles used for the sensitivity analysis: (black) smooth analytical expression; (green to brown) 10 m to 150 m deep 0.05 gr/cm^3 perturbations.

located at 12 m depth, compared to a reference (or *synthetic truth*) density profile where the perturbed layer is 20 m deep.

Some examples of the lag-holograms resulting from these perturbed profiles (with lag-to-lag and total power normalization) are displayed in Figure 103.

Figure 104 compiles the cost function S_C evaluated in steps of 1 meter deep perturbations, for reference profiles with perturbations at 10 to 90 meters depth (in steps of 10 meter), using the lag-by-lag normalization. Figure 105 repeats the same exercise for lag-holograms normalized by the total power.

If the model were a linear combination of its parameters, or anything closer to linear, the S_C functions would follow a parabolic well with its minimum at the *synthetic truth*. The location of the trough is the solution, whereas its curvature relates to the uncertainty. Non-linearity introduce a variety of effects, such as multiple troughs (potential multiple solutions–degenerated solution), or wide flat troughs (large uncertainty around the solution). The fact that this exercise deals only with the model, with no assumed mismodelling errors, neither noise, brings the minimum cost function value to zero. When evaluating S_C with real data (that is, when $Y_{\mathcal{W}}^{p_{ref}}$ is replaced by data-observables), the noise will mask the lower levels of our synthetic functional cost, and any systematic mismodelling might completely change the shape of them. This exercise must thus be seen as the sensitivity analysis of the model itself.

As shown in Figures 104 and 105, the functional costs might present some degree of degradation, with some multiple troughs appearing along the function. However, a minimum around the reference (*synthetic true*) is always present, with a typical width of $\leq$10 meter. The lag-by-lag normalization seems to better discern between features coming from deep layers, while the total power normalization performs better near the surface levels.

In spite of the non-linear aspect of the cost functionals evaluated in this section, and provided that the inversion approach scans only a small portion of the functional cost around the solution (a-priori close to the solution), we proceed with a linearized inversion of the layers in the next section.

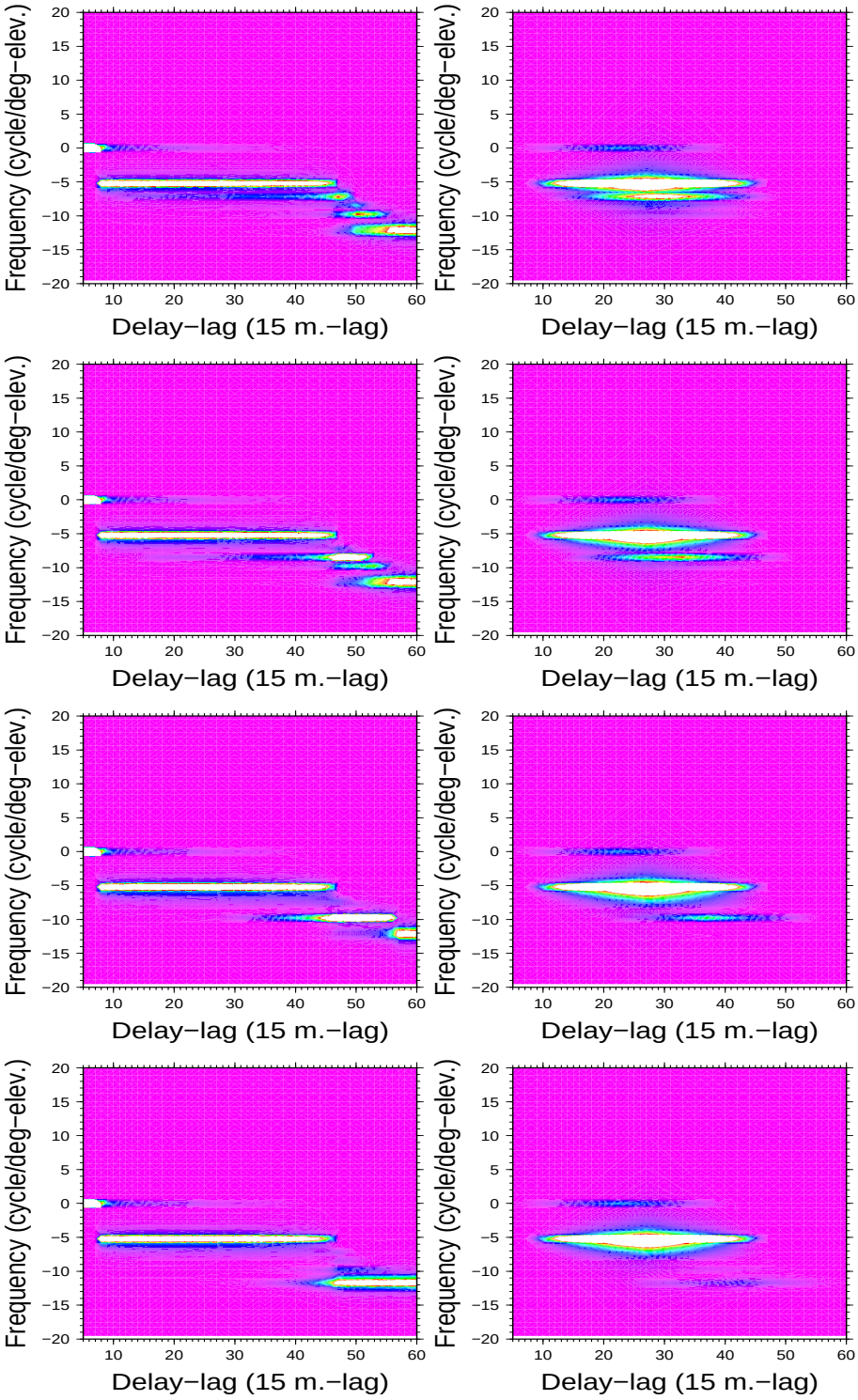

Figure 103.: Examples of lag-holograms produced with a smooth analytical profile, with a single sharp perturbed layer, as those shown in Figure 102. On the left, lag-by-lag normalization, on the right normalization by total power. Top to bottom, perturbed layer at 20, 40, 60, and 90 m respectively. The saturation of the color scale has been lowered to highlight the secondary features. Some of the frequency bands after lag 45 appearing on the lag-by-lag normalization are artifacts of the layer discretization (1 meter resolution). They are much weaker in the total power normalization approach.

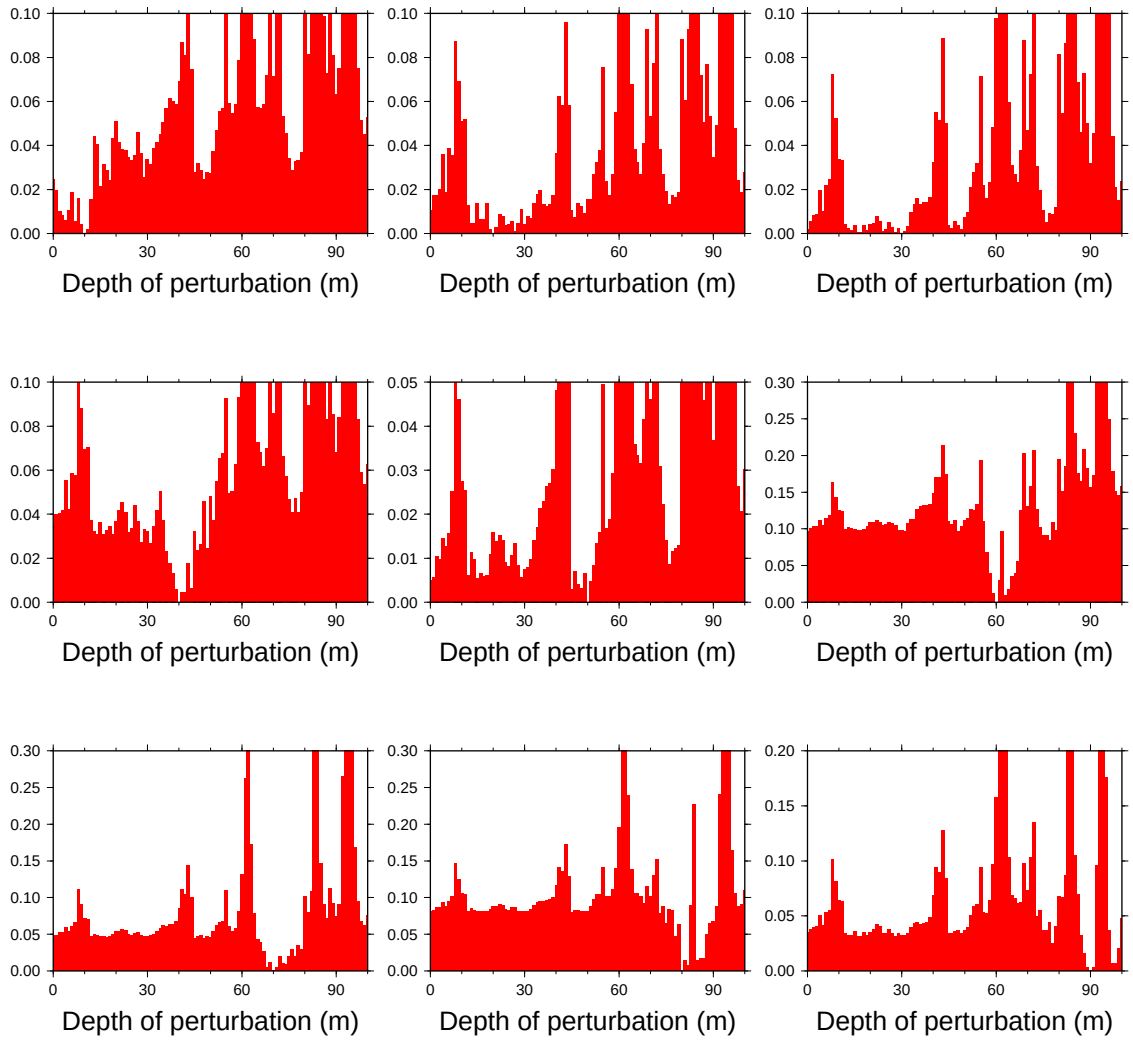

Figure 104.: Cost function (y-axis in arbitrary units) around reference density profiles with the perturbation located at 10 to 90 m depth in 10 m steps (left to right, top to bottom), using a lag-by-lag normalization. Please note different y-axis scales.

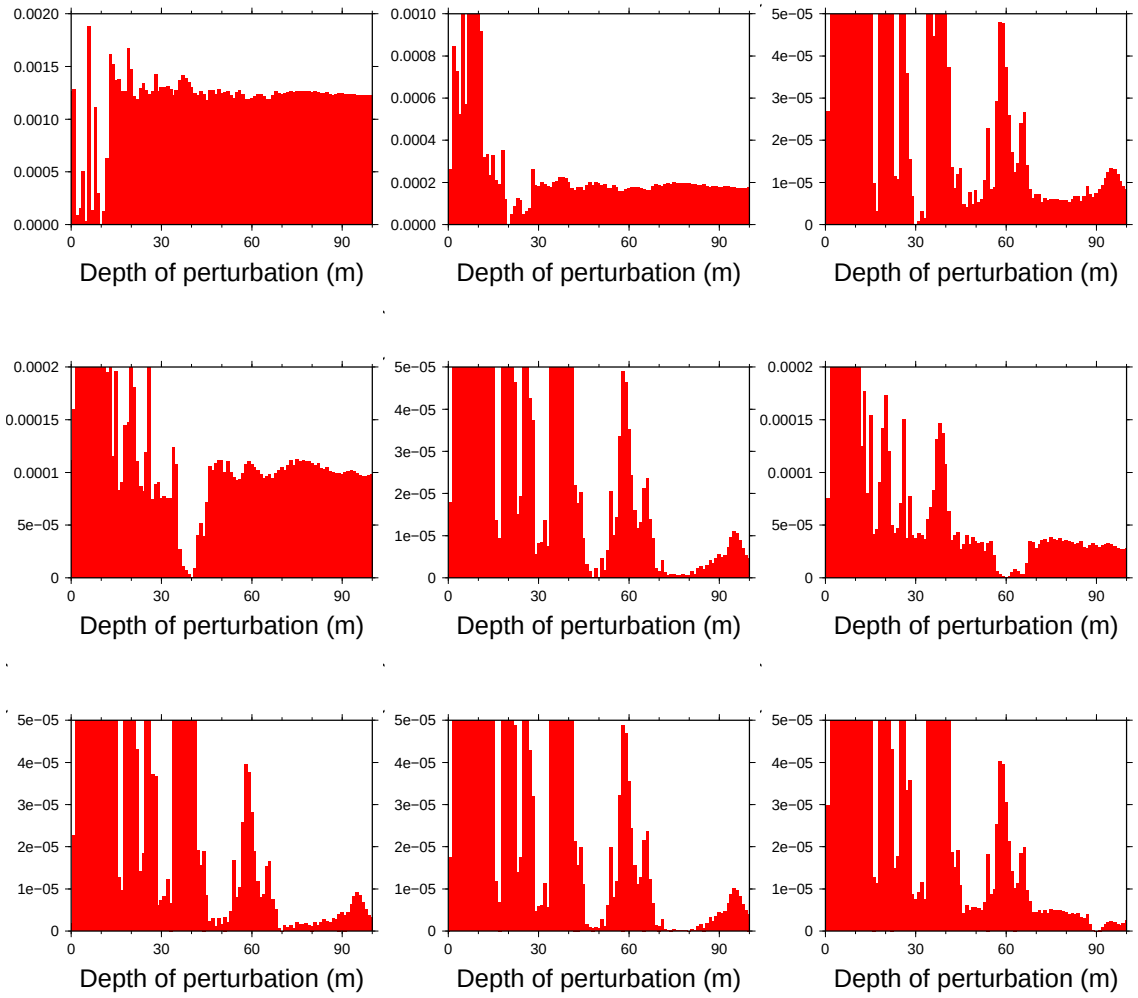

Figure 105.: Cost function (y-axis in arbitrary units) around reference density profiles with the perturbation located at 10 to 90 m depth in 10 m steps (left to right, top to bottom), using a total power normalization. Please note different y-axis scales.

5.2.4.2 *Linearized inversion*

The approach we followed is a linearization of the problem around an a-priori profile of snow layers. The observables, $Y_{\mathcal{W}}$ are the arranged elements of the lag-hologram. The unknowns of the problem are the densities of the snow at different layers, arranged also as a 1-D array of M elements:

$$X_\rho = \begin{bmatrix} \rho_{s1} \\ \rho_{s2} \\ \vdots \\ \rho_{sM} \end{bmatrix} \tag{109}$$

The examples we have run use 700 meter depth, at 1 meter sampling. The forward model developed in Sections 5.1.2 and 5.1.3 for lag-hologram construction would correspond to the f_L function in Equation (110):

$$Y_{\mathcal{W}} = f_L(X_\rho) \tag{110}$$

If we assume an a-priori value for the snow density profile, X_ρ^0, close enough to the real profile, and we call $Y_{\mathcal{W}}^0 = f_L(X_\rho^0)$, then:

$$Y_{\mathcal{W}} - Y_{\mathcal{W}}^0 = \frac{\partial f_L}{\partial X_\rho}_{X_\rho^0} (X_\rho - X_\rho^0) \tag{111}$$

or

$$\Delta Y_{\mathcal{W}} = F_L(\Delta X_\rho) \tag{112}$$

Where F_L is the matrix of the partial derivatives, numerically computed around the a-priori profile.

The first step to know whether this approach might work, is to check the capacity of the linearized forward model to reproduce the total forward model. That is, whether $f_L(X_\rho)$ is similar to $F_L(\Delta X_\rho) + Y_{\mathcal{W}}^0$.

We have checked the linearized forward model by means of a simple model. The a-priori X_ρ^0 is an analytical profile, plotted in black in the left panel in Figure 106, whereas the *true* profile X_ρ is similar to X_ρ^0, but with a Gaussian perturbation at the layers closest to the surface (green profile in the same panel).

The matrix of partial derivatives, F_L, has been computed around X_ρ^0. If the linearization approach is correct, then $F_L(\Delta X_\rho) + Y_{\mathcal{W}}^0$ should not differ significantly from $f_L(X_\rho)$. The results of this comparison are plotted at the right panel in Figure 106, in green the *ground truth* $f_L(X_\rho)$ and red for the linearized version $F_L(\Delta X_\rho) + Y_{\mathcal{W}}^0$.

The conclusion is that the linearized forward model works for simple and smooth profiles. This is the first requirement for the inversion to work.

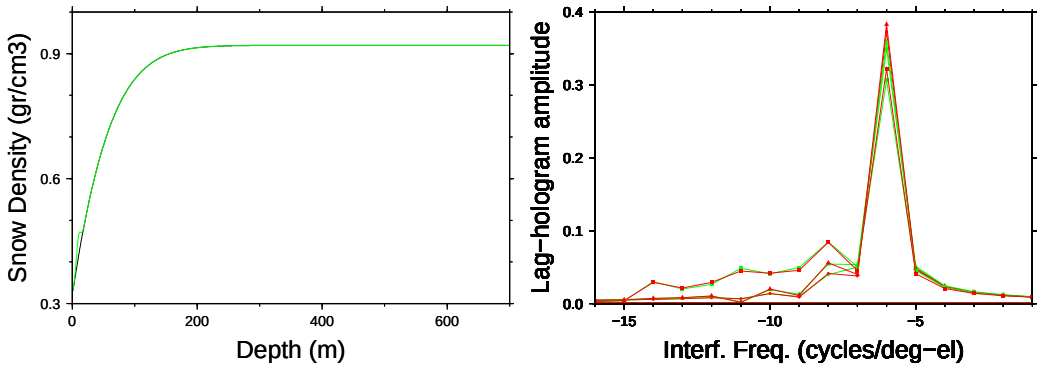

Figure 106.: [Left] Smooth profile used to check the linearization of the problem (green). The a-priori used to compute the matrix of partial derivatives is plotted in black. Note differences between 0 and 20 m. [Right] Different slices of the lag-hologram resulting from a *ground truth* snow density profile (green) and the resulting linearized forward model $F_L(\Delta X_\rho) + Y^0_{\mathcal{W}}$ (red). Circles for Lag 24, triangles for Lag 32, and squares for Lag 44.

5.2.4.3 *Outcome of the inversion*

The attempts to invert real data by using a linearized approach have not been fruitful. Different options have been tried:

- A non-weighted inversion (directly from Equation (112)):

$$\Delta X_\rho = (F_L^T F_L)^{-1} F_L^T \Delta Y_{\mathcal{W}} \tag{113}$$

  where the up-scripts ^{T} and $^{-1}$ mean the transpose and inverse matrix respectively.

- To account data covariance. When the noise of the data has been also considered, the solution becomes:

$$\Delta X_\rho = (F_L^T C_{\mathcal{W}}^{-1} F_L)^{-1} F_L^T C_{\mathcal{W}}^{-1} \Delta Y_{\mathcal{W}} \tag{114}$$

  where the data covariance is $C_{\mathcal{W}}$. The covariance of the solution is then $(F_L^T C_d^{-1} F_L)^{-1}$.

- Uncertainties in the a-priori model. When covariances have been also assumed for the a-priori model C_ρ, it then results in:

$$\Delta X_\rho = (F_L^T C_{\mathcal{W}}^{-1} F_L + C_\rho^{-1})^{-1} F_L^T C_{\mathcal{W}}^{-1} \Delta Y_{\mathcal{W}} \tag{115}$$

In general, the solution strongly relates to the a-priori, even when loose covariances are given. The unknowns have been defined as in the previous section (density of each layer, at certain resolution), playing with the resolution, the a-priori, and the covariances. A simpler approach has been also tackled, in which the unknowns were not the density layers, but coefficients of a degree-3 polynomial (4 unknowns). Similar problems have been found.

A possible explanation for this behavior might be given by the same reasons that could provoke the poor geographic consistency found in the lag-holograms and mentioned in Section 5.2.3: possible inhomogeneities in the dry snow profile across the scanned area (∼500 meter long); and the limited capability of the simple MRSR model to explain all the features in the data.

5.2.5 EXTRAPOLATION OF THE MODEL TO LINEAR POLARIZATIONS: APPLICATION TO DOMEX-2

In spite of being developed towards reflections from incident GPS-L1 RHCP signals, the forward model described in Section 5.1.2 can be easily adapted to other scenarios using signals with different characteristics in terms of polarization and frequency. In addition, if the wavelength does not differ so much from GPS-L1's (L-band), the permittivity properties would not significantly change and a similar behavior in terms of sub-surface reflections would be also expected.

We can consider a case study where a receiver collects signals reflected off the snow layers with linear polarizations (Vertical and Horizontal) at a frequency of 1413 MHz, placed 13 m high from the surface level. Adapting the receiver's height and frequency has no major difficulties than setting two parameters from the whole MRSR processing chain. Another correction that has to be made for the computation of the amplitude of the i-layer contribution described in Section 5.1.2.2 would be related to the Fresnel coefficients, where the transformations made from Equations (87) to (90) should be avoided to directly use Equations (83) to (86) by assigning Vertical to parallel ($\parallel$) and Horizontal to perpendicular ($\perp$) polarizations respectively. Let's consider also that the receiver's antenna has an orientation and beamwidth such as no direct signal from the transmitter is sensed. Therefore, the only modification to be made for the determination of delays described in Section 5.1.2.1 would be to set the reflected signal at the surface level (air/snow interface) as a reference to then compute each delay contribution from deeper layers with respect to it.

The characteristic mentioned above are not arbitrary chosen, since they correspond to those from DOMEX-2 campaign. As described in Appendix E.4, this experiment was carried on in Dome-C in 2008-2009 and 2009-2010 by IFAC and other scientific partners, with the aim of evaluating the long-time stability of L-band microwave emission of the snow surface by means of brightness temperature measurements taken by the L-band RaDomeX radiometer. However, coming back to our adaptation of the MRSR, there is no apparent reason for extrapolating a bistatic radar model with interferometric behavior produced by multiple sub-surface contributions, into a passive and more static (in terms of elevation dependency) scenario typical from radiometric observations. The following sub-sections provide the arguments which motivated this research and the preliminary results obtained by means of simulations.

5.2.5.1 *Unexpected behavior in radiometric observations: Sun fringes*

By assuming a stable dry snow scenario in terms of L-band microwave emission, the expected variability of the long term brightness temperature measurements should have mainly two types of dynamics, daily and seasonal, with a small variation at the surface level ($\sim 3K$) and related to the Sun's position (Macelloni et al., 2006). However, the results obtained shown periodic, fast and strong fluctuations in the horizontal component of the brightness temperature (T_h). A few examples are displayed on the top panel in Figure 135 (Appendix E.4). By analyzing the geometrical characteristics of the system, it was found that these unexpected events were always detected when a specular reflection of the Sun was entering the main beam of the antenna, as illustrated on the bottom panel

in Figure 135, where we can see the time coincidence between the moment when the Sun's Azimuth position crosses the receiver's orientation (and their elevation angles –or Zenith– are also close enough) and the occurrence of fast fluctuations. We thus define these events as "Sun fringes".

By checking the fast variability of T_h during the Sun fringes, we can conclude that this effect cannot be produced by a single reflection from the surface level given that, in such situation, the brightness temperature variation should rather manifest a smooth pattern proportional to the shape of the antenna's main beam. Moreover, the polarization discrepancy would neither be explained. On the other hand, the behavior of the Sun fringes would be better explained by an interferometric approach with multiple L-band Sun's reflections coming from sub-surface snow layers. In other words, the adaptation of the MRSR previously mentioned. In fact, notice that the fast fluctuations displayed on the top panel in Figure 135 during the Sun fringes show certain repeatability day after day, which could be given by some elevation-dependency, therefore being consistent with our hypothesis.

5.2.5.2 *Comparison between radiometric measurements and adapted MRSR*

In order to compare the brightness temperature variations during the Sun fringes with the output from the adapted MRSR, there is no reason to perform a lag-holographic analysis, given that the radiometric measurements correspond to absolute values related to the power of the received signal, thus no complex rotations would be available as in the GPS-R case. Therefore we directly check the power obtained from the adapted MRSR once corrected by the antenna gain-pattern (provided also by IFAC). As in the standard MRSR described in Section 5.1.2, the values are normalized to the incident wave upon arrival at the snow surface. The results obtained compared with several brightness temperature retrievals measured during Sun fringe events are displayed in Figures 107 to 112. Note that the days with low variability (March 16th and September 16th) correspond to periods where the Sun elevation is far from the antenna's pointing direction (at 48° of elevation).

From the seasonal variety of brightness temperature measurements provided by IFAC, we can see that there is general good agreement in the position of the most significant peak-fluctuations predicted by the simulations (with the only exception shown in the range 22 to 24° at the left panel in Figure 112). Moreover, it is specially relevant how the weaker response of the model in vertical polarization matches with the radiometric results. In addition, we can observe that when the Sun is at elevation low enough to be visible outside the main beam of the receiver's antenna (pointing towards 48° of elevation with a 3 dB beamwidth of $\sim$30°), no fluctuations are detected in T_h (neither in T_v), as displayed in Figures 109 and 110.

Regarding the amplitude of the peaks sensed by the radiometer during the Sun fringes, we could conclude that the degree of impact produced by the reflections might be related to the absolute brightness temperature measured. For instance, by comparing the results shown at the left panel in Figure 111 with those in Figure 108, we can see that modeled peak power levels around 0.007 (a.u.) produces a similar increment of T_h at 185K (October) than levels of 0.020 at 189K (February); similarly, the same simulations at 0.007 are barely sensed for T_v at 209K (February). Therefore, the higher the brightness tem-

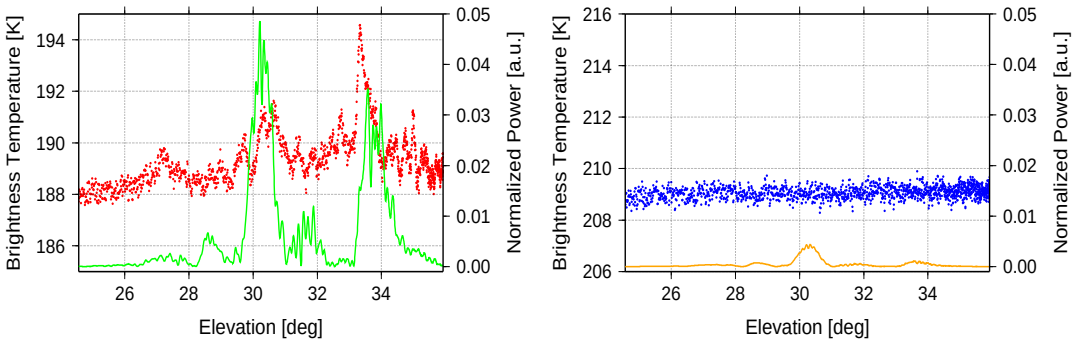

Figure 107.: [Left] Horizontal component of brightness temperature (T_h in red) measured with RaDomeX during 15/01/2010 compared with simulated Sun's reflected power using adapted MRSR and horizontal polarization (green) and applying the radiometer's antenna gain-pattern. [Right] The same comparison using Vertical component of brightness temperature (T_v in blue) and vertical polarization in the adapted MRSR model (orange). Note that the temperature's levels differ while keeping the same resolution. The elevation range chosen corresponds to the time moments when the Sun's Azimuth lies in the interval $\pm 35°$ with respect to the antenna's line-of-sight orientation (Azimuth= 315°). No fringes were found outside this interval.

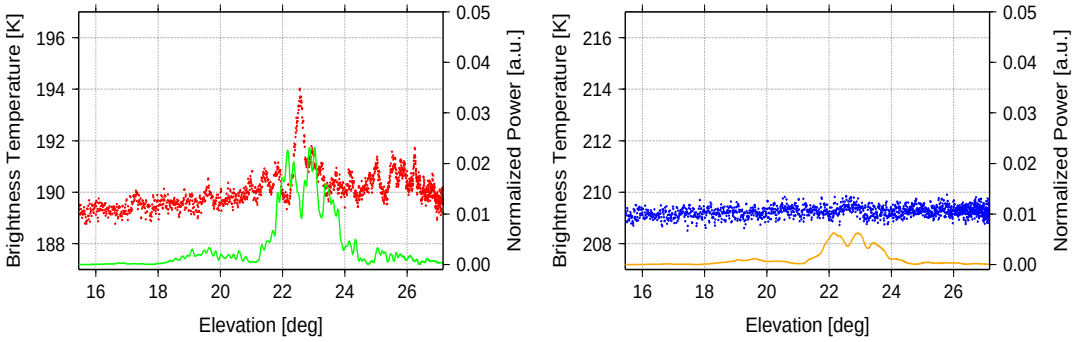

Figure 108.: The same type of representation as in Figure 107 but for 16/02/2010.

perature measured, the lower the impact produced by Sun reflections from the dry snow layers. Notice that this statement provides an additional argument for explaining the better robustness shown by the vertical component of brightness temperature during the Sun fringes events.

In spite of the promising preliminary results obtained, there are still some inconsistencies that should be analyzed and further research is required, which is out of the scope of this work. However, to find evidences of sub-surface interferometric behavior from the measurements made by a different architecture/system (at L-band, but not related to GPS) at the same experimental site, represents a supplementary justification for the investigation described along this Chapter towards remote sensing of dry snow.

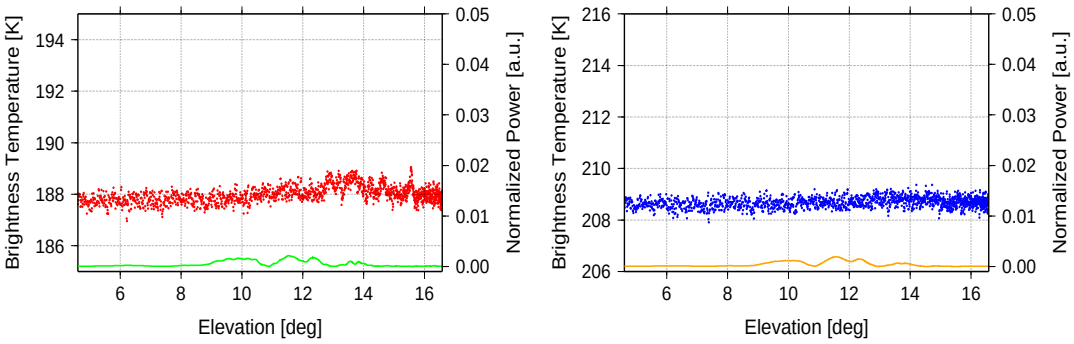

Figure 109.: The same type of representation as in Figure 107 but for 16/03/2010.

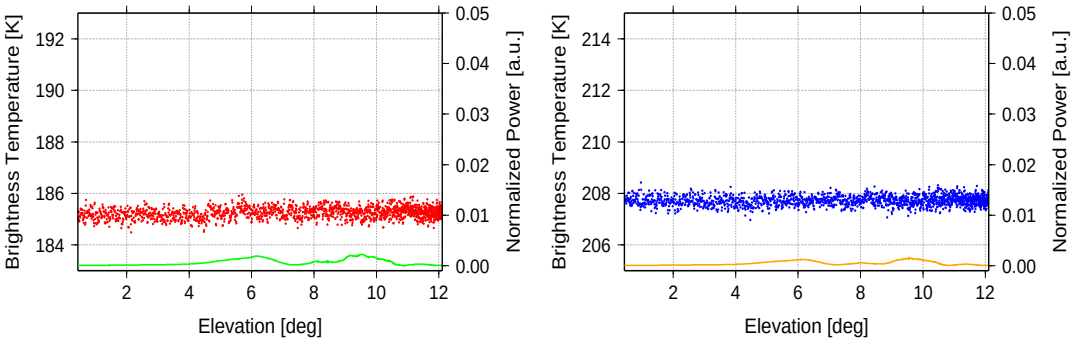

Figure 110.: The same type of representation as in Figure 107 but for 16/09/2010.

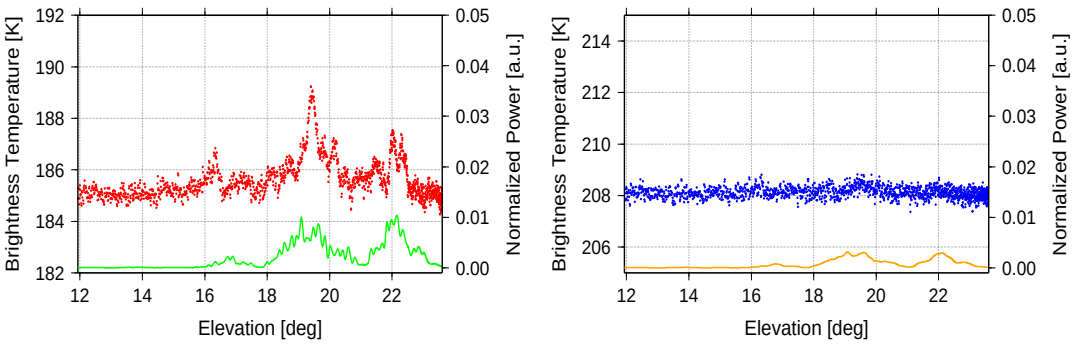

Figure 111.: The same type of representation as in Figure 107 but for 16/10/2010.

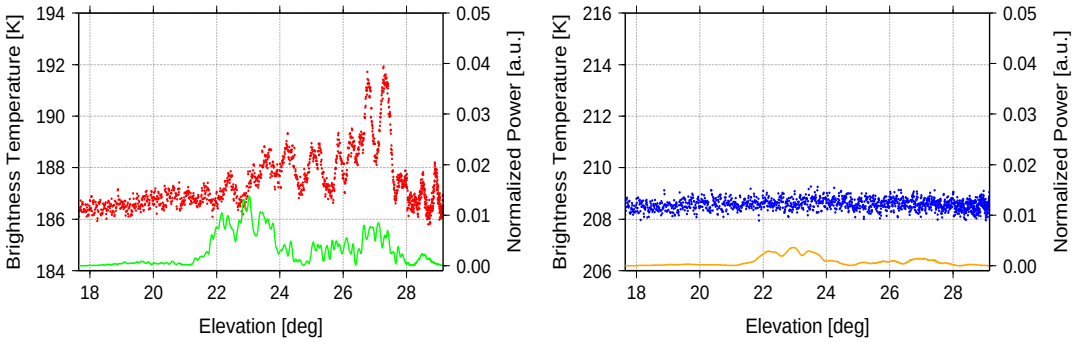

Figure 112.: The same type of representation as in Figure 107 but for 01/11/2010.

5.2.6 EXTRAPOLATION TO A SPACEBORNE SCENARIO

Even thought the results of this experiment show the potential sensing of dry snow subsurface signatures with reflected GPS signals from a fixed platform, the final application of this technique should be performed from satellite receivers in order to achieve wider coverage. The extrapolation of this results to a spaceborne scenario is therefore needed.

A first consideration is that the peak power of the waveforms will be substantially lower, due to higher propagation losses and the signal's spreading over range delay and frequency shifts (increase of the glistening area). In Wiehl et al. (2003), a decrease of $\sim$20 dB is obtained when going from an aircraft scenario (4 km height and 200 m/s speed) to a LEO satellite case (400 km height and 7.6 km/s speed) in simulations over Antarctica. Despite that this work is done using P-code waveforms and considering the subsurface contributions as volume scattering, similar results can be expected from our case (the influence of the direct signal impairs us to perform the same analysis over the dataset obtained). The immediate conclusion that we can get is that a hight gain antenna is required, which means a high directivity. Taking into account that at the same time, different elevation angles of observation are desired for achieving spatial coverage (in general) or for generating the lag-holograms (in our particular case), a beamforming strategy like in Martín-Neira et al. (2011) seems to be the best option.

With hundreds of kilometers of distance from the surface level, the direct and reflected signals do not overlap, and will also have largely different Doppler values. This impedes the use of the direct signal to stop the reflected one. In absence of a better reference to stop the reflected signals, during a first iteration, a counter-rotator phasor should be generated using the surface-reflected path delay computed from the positions of receiver&transmitter plus a model of the Earth's surface (e.g. geoids or surface elevation models). Note that this is the approach taken in the Sun fringes study.

Another aspect to be considered in dynamic scenarios–with respect to fixed-platforms–is time-varying topography. Simulations done in Wiehl et al. (2003) show how the waveform's shape is perturbed by the effect of a topographic slope, where there is a shift towards a frequency sense depending on the directions of the slope and the trajectory of the satellite, which can be detected by means of delay-Doppler maps.

Regarding Doppler effects, the velocity of the receiver in a LEO satellite ($\sim$7.5 km/s) might lead to different Doppler-frequency contributions over the reflecting ground region (non-specular reflections). However, previous experiments with real GPS reflections (Lowe et al., 2002a; Gleason, 2010) show how these frequencies can be properly determined from space.

Another concern is the spatial resolution of the present technique in a satellite platform. Basically, the analysis shown along Section 5.1 is based on computing Fourier transforms of waveform series, long enough to include variation in the elevation angle, in order to separate the contributions to the reflected signal coming below the surface level. The depth resolution depends on the rate of elevation's variation and on the length of the data series (which determines the resolution in the frequency domain for a given sampling rate). With the receiver inside a LEO satellite, we can assume that the elevation angle and elevation-rate is dominated by the GPS transmitter. However, the speed of the specular footprint determines the minimum ground track (spatial range) to obtain the number of data samples for the FFT algorithm, and it depends on the receiver, with a typical value of

7.5 km/s. Notice that in our analysis, we assume that the internal layering is constant for the whole data series, which is a valid statement with local measurements from a fixed platform, but it seems unrealistic from space due to the large spatial ranges required. This effect would make the retrieval much more challenging, or different approaches should be investigated.

Finally, taking into account that our methodology requires phase determination, the coherence of the signal from GPS reflections over dry snow masses collected from space-borne receivers should be properly studied. That includes also the effect of speckle noise and the impact of roughness. To asses this problem is not straightforward and it remains as an open question that will require a deeper analysis.